Characterization of a CO_2 Dipole Trap of ^{87}Rb as Part of an Ultra-cold Atom-Ion Interaction Experiment

Elad Kronstein

Abstract

This work describes the characterization of a single focused beam CO_2 dipole trap for cold Rubidium atoms. This trap is part of a set-up that is designed for studying the interaction between ultra-cold neutral atoms and one or several atomic ions in a Paul trap. The purpose of the dipole trap in the experiment is to achieve high atomic phase-space densities and reach quantum degeneracy through forced evaporation. The use of all-optical means in order to achieve this goal is resilient against the RF fields emanating from the ion Paul trap, as would be the case in a magnetic trap. The CO_2 trap has an extremely low spontaneous photon scattering rate, hence trapping does not fundamentally introduce heating to the atoms. The extreme detuning allows trapping of atoms independent of their internal state and the trapping of more than one species, an important feature in future experiments with ultra-cold ensembles of ^{88}Sr.

In this thesis we describe the work we performed to characterize a Magneto-Optic trap (MOT) that served as a source of cold Rb atoms, the performance of laser-cooling and the loading and performance of a CO_2 trap. Among various techniques, we have used microwave spectroscopy to analyze the atomic ensembles at different stages of the experiment. We found that the life-time of the atoms in the trap was too short to enable forced evaporation to quantum degeneracy. The trap lifetime was limited by collisions with background thermal atoms in the chamber due to background pressure. As a result the system was disassembled for vacuum improvements.

Contents

1 Introduction

The development of laser and other cooling techniques in atomic gases has triggered extensive experimental and theoretical work in the field of interactions between neutral atoms in the ultra-cold regime [25]. These Van der Waals interactions are short-ranged and scale as $V(r) \sim -1/r^6$ $@r \rightarrow \infty$. The short potential range as compared with the atomic thermal de Broglie wavelength at the ultra-cold temperature regime results in collisions that are governed by S-wave scattering, for which only one parameter, the scattering length, determines all of the interaction properties. The interactions between two or several trapped and laser-cooled ions was investigated as well. Here, the interaction is long-ranged obeying the Coulomb potential law $V(r) \sim -1/r$ $@r \rightarrow \infty$. Due to the longer range several laser-cooled and trapped ions form a Wigner crystal with well defined equilibrium positions [27]. Interactions between ions in these crystals were studied using up to $\sim 10^5$ ions[28, 29]. The study of ultra-cold atom-ion interactions is in its infancy. Interactions of ions with neutral atomic clouds had been studied in the mK regime [30, 31], and only recently with Bose-Einstein condensates [32, 33]. The interaction potential characterizing atom-ion interactions is a polarization potential in which the charged ion's electric field polarizes the neutral atom. Here the interaction potential scales as $V(r) \sim -1/r^4$ $@r \rightarrow \infty$, resulting in a longer interaction range. As a result, the s-wave regime, in which only a single partial wave contributes to a collision requires cooling to the sub μK temperature range. A number of theoretical works analyzing ultra-cold atom-ion collisions were published [35, 38, 34, 36, 37]. Understanding elastic collisions in this regime is necessary for achieving and optimizing sympathetic cooling of species which do not allow direct laser cooling, for example, complex molecules. On the other hand, inelastic collisions in this regime provide the opportunity to observe quantum mechanical details of chemical processes which are typically averaged out at higher temperatures [39]. In addition, interesting phenomena such as charge exchange collisions [34] and novel atom-ion bound states [40] may be investigated. An application of using the ion to probe the local density profile of the atomic cloud may allow for probing with better resolution then the conventional optical methods.

This work describes a characterization of the CO_2 dipole trap which is the part in the full experiment responsible for the cooling of the neutral atoms to quantum degeneracy. The use of such an all-optical approach instead of the conventional magnetic trap was chosen because of its insensitivity to stray RF fields that may originate from the ion Paul trap in the future experiment. It is also a relatively simple way of achieving quantum degeneracy. Bose-Einstein condensate formation in a CO_2 trap was first realized a decade ago [41] and since then several groups adopted this method [16, 18]. The use of a CO_2 laser to produce the dipole trap is convenient due to the high intensity of a few tens of Watts achievable, at relatively low cost the very long wavelength of $10.6\mu m$ allows a tight focus in the axial as well as in the radial direction. The tight focusing capability allows the use of a single beam trap instead of a crossed beam or a standing wave type, a configuration which is not applicable for example in YAG laser dipole traps.

In addition to the characterization of the dipole trap, the characterization of the magneto-optical trap (MOT) from which the dipole trap is loaded was also performed and reported. MOT optimization is a crucial part in optimizing the loading efficiency and initial temperature of the dipole trap.

Finally experiments in which RF spectroscopy of both the atoms in the MOT and in the dipole trap was performed, are presented as part of their characterization.

1.1 Thesis Layout

The next section describes the theory necessary to understand the principles of operation of both the dipole trap and the MOT. In Sec. 3, our experimental setup is described. Secs. 4 and 5 describe our measurements characterizing the traps and the performance of RF spectroscopy.

2 Theoretical Background

The following section is a theoretical discussion on the forces which due to interaction between a neutral atom and a laser field in the two-level approximation and it closely follows . The forces are divided to two types - a *dissipative force*, also known as the *scattering force* which is due to scattering of photons by the atom and a *reactive force*, also known as the *dipole force*, which can be described as a gradient of a potential, therefore it is of conservative nature. Two limits are of major importance: the near resonance limit, relevant for describing laser cooling and magneto-optical trapping (MOT) mechanisms and the *Quasi-electrostatic* limit, in which the detuning of the trapping laser is of the order of the atomic resonance, relevant for the description of a CO_2 dipole trap operation for ^{87}Rb atoms.

2.1 Two-Level Atoms in Laser Light

In the two-level approximation we consider only two levels of the atom $|e\rangle$ and $|g\rangle$ separated by an energy $\hbar\omega_A = E_e - E_g$. The two levels are coupled by laser light while transition amplitudes to other levels are negligible. Such an approximation is valid when the laser is farther off-resonance with respect to other allowed transitions. We also use a semi-classical approach in which the laser field is treated classically and only the vacuum state is considered quantum mechanically. The System's Hamiltonian H, is then given by,

$$H = H_A + H_V + V_{AL} + V_{AV}. \tag{2.1}$$

Here H_A is the atom Hamiltonian, composed of external and internal degrees of freedom Hamiltonians,

$$H_A = H_A^{ext} + H_A^{int} = \frac{\mathbf{P}^2}{2M} + \hbar\omega_A|e\rangle\langle e|. \tag{2.2}$$

The vacuum field Hamiltonian H_V is given by,

$$H_V = \sum_j \hbar\omega_j \left(a_j^\dagger a_j + \frac{1}{2} \right). \tag{2.3}$$

Here $a_j^\dagger a_j$ is the field's photon number operator in mode j, of energy $\hbar\omega_j$. We assume the field is initially in the vacuum state , i.e. $\langle a_j^\dagger a_j \rangle = 0$ for all j. The laser field is considered monochromatic with angular frequency ω_L and given by

$$\mathbf{E}_L\left(\mathbf{r},t\right)=\vec{\epsilon}\left(\mathbf{r}\right)E_0\left(\mathbf{r}\right)\cos\left(\omega_L t+\Phi\left(\mathbf{r}\right)\right). \tag{2.4}$$

Here $\vec{\epsilon}\left(\mathbf{r}\right)$, $E_0\left(\mathbf{r}\right)$ and $\Phi\left(\mathbf{r}\right)$ are the laser field's polarization, amplitude and phase respectively. The interaction V_{AL}, generating photo absorption and stimulated emission, is

$$V_{AL}=-\mathbf{d}\cdot\mathbf{E}_L. \tag{2.5}$$

Here $\mathbf{R}$ is the atom's center of mass position which is also treated classically and $\mathbf{d}$ is the dipole operator of the atom, $\mathbf{d}=d\epsilon_z\left(|e\rangle\langle g|+|g\rangle\langle e|\right)$. We apply the *rotating wave approximation* (RWA), i.e. we drop the anti-resonant terms in V_{AL} and end up with

$$V_{AL}=\frac{\hbar\Omega\left(\mathbf{r}\right)}{2}\left[e^{-i\Phi(\mathbf{R})}e^{-i\omega_L t}|e\rangle\langle g|+h.c.\right]. \tag{2.6}$$

The RWA approximation is valid when the detuning $\delta=\omega_L-\omega_A$ satisfies $\delta\ll\omega_A,\omega_L$. The *Rabi frequency,* $\Omega\left(\mathbf{r}\right)$ is given by $\hbar\Omega\left(\mathbf{r}\right)=-dE_0\left(\mathbf{r}\right)\epsilon_z\cdot\epsilon\left(\mathbf{r}\right)$. Finally, the interaction Hamiltonian between the vacuum field and the atom is given by,

$$V_{AV}=-\mathbf{d}\cdot\mathbf{E}\left(\mathbf{R}\right), \tag{2.7}$$

where $\mathbf{E}\left(\mathbf{R}\right)$ is the quantum mechanical electromagnetic field operator

$$\mathbf{E}\left(\mathbf{r}\right)=i\sum_j E_j a_j\epsilon_j e^{i\mathbf{k}_j\cdot\mathbf{r}}+h.c. \tag{2.8}$$

and the quantum mechanical field is considered to be initially in the vacuum state. Here a_j is an annihilation operator of a photon with momentum $\hbar\mathbf{k}_j$, energy $\hbar\omega_j=\hbar ck_j$ and polarization ϵ_j. E_j is a normalization constant equal to

$$E_j=\sqrt{\frac{\hbar\omega_j}{2\epsilon_0 L^3}} \tag{2.9}$$

and is considered as the electric field amplitude corresponding to one photon of the mode j. L is the quantization length. The RWA is also applied to V_{AV}, i.e. neglecting the terms $a_j|g\rangle\langle e|$ and h.c..

2.1.1 Heisenberg's Equation of Motion

We are interested in the dynamics of the center of mass of the atom. Heisenberg's equation of motion for $\mathbf{R}$ and $\mathbf{P}$, the position and momentum operators of the atom's center of mass respectively, is

$$\dot{\mathbf{R}} = \frac{1}{i\hbar}\left[\mathbf{R}, H\right] = \frac{\partial H}{\partial \mathbf{P}} = \frac{\mathbf{P}}{M} \tag{2.10}$$

then the operator for the force acting on the atom is

$$\mathbf{F}\left(\mathbf{R}\right) = \dot{\mathbf{P}} = M\ddot{\mathbf{R}} = \frac{1}{i\hbar}\left[\mathbf{P}, H\right] = -\nabla V_{AL}\left(\mathbf{R}\right) - \nabla V_{AV}\left(\mathbf{R}\right) \tag{2.11}$$

The time dependence of the quantum electric field operator $\mathbf{E}\left(\mathbf{R}\right)$ appearing on the right hand-side of Eq. 2.11 in $\nabla V_{AV}\left(\mathbf{R}\right)$, is calculated using the transformation [2], $a_j\left(t\right) = a_j\left(0\right)e^{-i\omega_j t} + a_j^{source}\left(t\right)$, we can therefore express $\mathbf{E}\left(\mathbf{R}\right)$ as a sum of two terms, $\mathbf{E}\left(\mathbf{R}, t\right) = \mathbf{E}^{vac}\left(\mathbf{R}, t\right) + \mathbf{E}^{source}\left(\mathbf{R}, t\right)$. The source term, $\mathbf{E}^{source}\left(\mathbf{r}, t\right)$, is the electric field due to the atomic dipole moment induced by the vacuum field at the atomic position $\mathbf{R}$. It can be shown that $\mathbf{E}^{source}\left(\mathbf{r}, t\right)$ has no gradient at $\mathbf{R}$, the position of the atomic dipole moment, since it is an even function of $\mathbf{r} - \mathbf{R}$ [2]. Then the term $-\nabla V_{AV}\left(\mathbf{R}\right)$ describes the force due to momentum transfer from the atom to the vacuum field through photon spontaneous emission into unoccupied modes of the electromagnetic field, due to the atom's interaction with the vacuum field $\mathbf{E}^{vac}\left(\mathbf{R}, t\right)$. The term $-\nabla V_{AL}\left(\mathbf{R}\right)$, describes the force due to the atom-laser interaction in which momentum is transferred from the laser field to the atom and vice verse by photon absorption and stimulated emission processes respectively.

2.1.2 Time Scales and the Semi-classical Limit

In order to treat separately the time evolution of the internal and external degrees of freedom, there must be two very different time scales for each, such that one can adiabatically eliminate the fast degrees of freedom and average them out. Than one can treat the internal degrees of freedom phenomenologically. The time scale of the vacuum field degrees of freedom evolution is of the order $\tau_c \approx \frac{1}{\omega_A}$ which is

$\sim 10^{-17} sec$ in our case [3]. This time scale is much shorter than any time scale of the system, therefore one can regard the vacuum field as a reservoir and its effect is described as a relaxation process. The atom's internal degrees of freedom are characterized by the radiative time $T_{int} = 1/\Gamma$ which is the life time of an atom in the excited state $|e\rangle$ where Γ is the atom's line-width. The lifetime is finite due to spontaneous emission induced by the vacuum field. In our case $T_{int} \sim 26 \times 10^{-9} sec$, then $\Gamma \sim 2\pi \times 6MHz$. The time scale associated with the external degrees of freedom is given by $T_{ext} = \hbar/E_R$ where $E_R = \hbar^2 k_L^2/2M$ is the recoil energy. T_{ext} is the damping time of the atomic momentum. For most atomic transitions as in our case $\hbar\Gamma \gg E_R$ which implies that

$$T_{ext} \gg T_{int} \tag{2.12}$$

In our system $E_R/\hbar \approx 2\pi \times 3.8KHz$ so the condition 2.12 applies.

When treating the equations of motion semi-classically we regard the atom as well localized within the laser radiation field around $\mathbf{r}_0 = \langle \mathbf{R} \rangle$ and $\mathbf{p}_0 = \langle \mathbf{P} \rangle$. The atom can be considered well localized when the spread in position is much smaller that the laser wavelength,

$$\Delta\mathbf{R} \ll \lambda_L \tag{2.13}$$

and the spread of the Doppler shift is negligible compared to Γ, which implies that

$$k_L \delta v = \frac{k_L \Delta\mathbf{P}}{M} \ll \Gamma \tag{2.14}$$

Condition 2.13 is kept throughout the experiment due to photon scattering by the atom (see [4]). Equation 2.14 and 2.14 together with the Heisenberg inequality $\Delta\mathbf{R} \cdot \boldsymbol{\Delta}\mathbf{P} \geq \hbar$ result in the compatibility condition

$$\frac{\hbar k_L^2}{M} \ll \Gamma \tag{2.15}$$

which is equivalent to $E_R \ll \hbar\Gamma$ or $T_{ext} \gg T_{int}$. We find that the existence of two different time scales is necessary for the semi-classical picture to be valid.

2.1.3 The Mean Force

As mentioned in the previous section, we consider our system to be well described by the semi-classical limit. Then the external degrees of freedom of the atom $\mathbf{R}(t)$ and $\mathbf{P}(t)$ are replaced by the the numbers $\mathbf{r}(t)$ and $\mathbf{p}(t)$ respectively. Then the force operator in Eq. 2.11 acts only on the atom's internal degrees of freedom and the vacuum field degrees of freedom. We are interested in the mean force acting on the atom

$$\mathcal{F}(\mathbf{r},t) = \langle \mathbf{F}(\mathbf{r},t) \rangle = -\langle \nabla V_{AL}(\mathbf{r},t) \rangle \tag{2.16}$$

The second term on the right hand side of Eq. 2.11 vanishes because there is no momentum transfer between the atom and the vacuum field due to the inversion symmetry of the spontaneous emission process. Under the semi-classical approximation, Eq. 2.6 becomes

$$-\nabla V_{AL}(\mathbf{r},t) = -\frac{\hbar}{2}|e\rangle\langle g|e^{-i\omega_L t}\nabla\left[\Omega(\mathbf{r})\,e^{-i\Phi(\mathbf{r})}\right] + h.c. \tag{2.17}$$

The gradient of Eq.2.17 can be written as

$$\nabla\left[\Omega(\mathbf{r})\,e^{-i\Phi(\mathbf{r})}\right] = \Omega_1(\mathbf{r})\,e^{-i\Phi(\mathbf{r})}\left[\frac{\nabla\Omega(\mathbf{r})}{\Omega(\mathbf{r})} - i\nabla\Phi(\mathbf{r})\right] \tag{2.18}$$

The mean value of $|e\rangle\langle g|$ is $\sigma_{ge}(t)$ where σ is the internal atomic density operator. Then the mean force assumes the form

$$\mathcal{F}(\mathbf{r},t) = -\hbar\Omega(\mathbf{r})\left[u(t)\frac{\nabla\Omega(\mathbf{r})}{\Omega(\mathbf{r})} + v(t)\nabla\Phi(\mathbf{r})\right]$$

with

$$u(t) = \mathrm{Re}\,\sigma_{ge}(t)\,e^{-i[\omega_L t+\Phi(\mathbf{r})]} \tag{2.19a}$$

$$v(t) = \mathrm{Im}\,\sigma_{ge}(t)\,e^{-i[\omega_L t+\Phi(\mathbf{r})]} \tag{2.19b}$$

We are left with evaluating σ. The equation of motion for σ is

$$\dot{\sigma} = \frac{1}{i\hbar}[H,\sigma] \tag{2.20}$$

Where H is the full Hamiltonian as described in Eq. 2.1. σ commutes with the atom's external degrees of freedom Hamiltonian H_A^{ext} and with H_V. Since we treat the vacuum as a reservoir, we replace V_{AV} by a phenomenological damping term. Then Eq. 2.20 for the matrix element σ_{ab} becomes

$$\dot{\sigma}_{ba} = \frac{1}{i\hbar}\langle b|\left[H_A^{int} + V_{AL}, \sigma\right]|a\rangle + \left(\frac{d}{dt}\sigma_{ba}\right)_{sp} \tag{2.21}$$

Where $\left(\frac{d}{dt}\sigma_{ba}\right)_{sp}$ is the damping term and it describes the decay of the excited state to the ground state and the decay of the optical coherence of σ, $\left(\frac{d}{dt}\sigma_{ee}\right)_{sp} = -\Gamma\sigma_{ee}$, $\left(\frac{d}{dt}\sigma_{gg}\right)_{sp} = +\Gamma\sigma_{ee}$, $\left(\frac{d}{dt}\sigma_{eg}\right)_{sp} = -\frac{\Gamma}{2}\sigma_{eg}$ and $\left(\frac{d}{dt}\sigma_{ge}\right)_{sp} = \frac{\Gamma}{2}\sigma_{ge}$, where Γ is the decay rate of the excited state. Since $\sigma_{ee} + \sigma_{gg} = 1$, the four equations described in Eq. 2.21 reduce to three. Defining the population inversion variable as

$$w = \frac{1}{2}\left(\sigma_{ee} - \sigma_{gg}\right) \tag{2.22}$$

and according to Eq. 2.21 and the definition Eq. 2.19a and 2.19b of $u\left(t\right)$ and $v\left(t\right)$ we result with the *Optical Bloch Equations* (OBE)

$$\begin{pmatrix} \dot{u} \\ \dot{v} \\ \dot{w} \end{pmatrix} = \begin{pmatrix} -\frac{\Gamma}{2} & \delta + \dot{\Phi} & 0 \\ -\left(\delta + \dot{\Phi}\right) & -\frac{\Gamma}{2} & -\Omega \\ 0 & \Omega & -\Gamma \end{pmatrix} \begin{pmatrix} u \\ v \\ w \end{pmatrix} + \begin{pmatrix} 0 \\ 0 \\ -\frac{\Gamma}{2} \end{pmatrix} \tag{2.23}$$

Notice that $\dot{\Phi} = \frac{d\mathbf{r}}{dt} \cdot \nabla\Phi = \frac{d\mathbf{r}}{dt} \cdot \beta$ where $\frac{d\mathbf{r}}{dt}$ is the atom's velocity. For an atom at rest, $\dot{\Phi} = 0$ and the OBE become a set of coupled linear differential equations with time independent coefficients. Therefore it has a steady state solution, which is given by

$$u_{st} = \frac{\delta}{\Omega}\frac{s}{s+1} \tag{2.24a}$$

$$v_{st} = \frac{\Gamma}{2\Omega}\frac{s}{s+1} \tag{2.24b}$$

$$w_{st} = -\frac{1}{2\left(1+s\right)} \tag{2.24c}$$

where

$$s = \frac{\Omega^2/2}{\delta^2 + \left(\frac{\Gamma^2}{4}\right)} \tag{2.25}$$

is the saturation parameter. The steady state force is then

$$\mathcal{F}_{st}\left(\mathbf{r}, t\right) = -\hbar\Omega\left(\mathbf{r}\right)\frac{s}{s+1}\left[\delta\frac{\nabla\Omega\left(\mathbf{r}\right)}{\Omega^2\left(\mathbf{r}\right)} + \frac{\Gamma}{2\Omega}\nabla\Phi\left(\mathbf{r}\right)\right] = \mathcal{F}_{dipole} + \mathcal{F}_{scatt} \tag{2.26}$$

As mentioned earlier, it is composed of a sum of two forces, the *dipole force* and the *scattering force.*

2.2 The Scattering Force

According to Eq. 2.26, the scattering force is

$$\mathcal{F}_{scatt} = -\hbar\frac{s}{s+1}\frac{\Gamma}{2}\nabla\Phi\left(\mathbf{r}\right) = -\hbar\frac{\Gamma}{2}\nabla\Phi\left(\mathbf{r}\right)\frac{\Omega^2/2}{\delta^2 + (\Gamma^2/4) + (\Omega^2/2)} \tag{2.27}$$

For a plane wave laser field,$\Phi = -\mathbf{k}_L \cdot \mathbf{r}$, then the scattering force is

$$\mathcal{F}_{scatt} = \hbar\mathbf{k}_L\frac{\Gamma}{2} \cdot \frac{\Omega^2/2}{\delta^2 + (\Gamma^2/4) + (\Omega^2/2)} \tag{2.28}$$

Defining the zero-detuning saturation parameter, s_0 and the saturation intensity, I_s as

$$s_0 = 2\left(\frac{\Omega}{\Gamma}\right)^2 = \frac{I}{I_s} \tag{2.29}$$

one finds that

$$\frac{\Omega^2/2}{\delta^2 + (\Gamma^2/4) + (\Omega^2/2)} = \frac{s_0}{1 + s_0 + 4\left(\frac{\delta}{\Gamma}\right)^2}$$

and then

$$\mathcal{F}_{scatt} = \hbar\mathbf{k}_L\frac{\Gamma}{2} \cdot \frac{s_0}{1 + s_0 + 4\left(\frac{\delta}{\Gamma}\right)^2} \tag{2.30}$$

This force is often called *radiation pressure.* Each photon from the laser carries a momentum $\hbar\mathbf{k}_L$, therefore from Eq. 2.28 it is evident that the photon scattering rate by the atom is

$$\frac{dN}{dt} = \frac{\Gamma}{2} \frac{s_0}{1 + s_0 + 4\left(\frac{\delta}{\Gamma}\right)^2} \tag{2.31}$$

In the limit of infinite laser intensity ($\Omega^2 \to \infty$), the scattering rate reaches a maximum value $\left(\frac{dN}{dt}\right)_{max} = \frac{\Gamma}{2}$, and the maximal force is accordingly $\mathcal{F}_{scatt}^{max} = \hbar \mathbf{k}_L \frac{\Gamma}{2}$. This type of force is used for cooling due its non conservative nature.

In case of a moving atom with velocity $\mathbf{v}$ in a plane wave with direction $\mathbf{k}$, in the atom's rest frame the laser frequency is Doppler shifted while the Rabi frequency is still time independent. Therefore there is a steady state solution of Eqs. 2.23 and it is obtained by shifting the detuning by the Doppler shift in Eq. 2.28:$\delta \to \delta - \mathbf{k} \cdot \mathbf{v}$. Then the force becomes

$$\mathcal{F}_{scatt} = \hbar \mathbf{k}_L \frac{\Gamma}{2} \cdot \frac{s_0}{1 + s_0 + 4\left(\frac{\delta - \mathbf{k} \cdot \mathbf{v}}{\Gamma}\right)^2} \tag{2.32}$$

Note that the maximal force is obtained for $\delta = \mathbf{k} \cdot \mathbf{v}$.

2.3 The Dipole Force

According to Eq. 2.26, the dipole force is given by

$$\mathcal{F}_{dipole} = -\hbar \frac{s}{s+1} \delta \frac{\nabla \Omega(\mathbf{r})}{\Omega(\mathbf{r})} = -\hbar \delta \frac{\nabla \Omega(\mathbf{r})}{\Omega(\mathbf{r})} \frac{\Omega^2(\mathbf{r})/2}{\delta^2 + (\Gamma^2/4) + (\Omega^2(\mathbf{r})/2)} \tag{2.33}$$

This force is conservative, since it can be written as

$$\mathcal{F}_{dipole} = -\nabla U(\mathbf{r})$$

where

$$U(\mathbf{r}) = \frac{\hbar \delta}{2} \ln\left(1 + \frac{\Omega^2(\mathbf{r})/2}{\delta^2 + (\Gamma^2/4)}\right) \tag{2.34}$$

In the derivation of Eqs. 2.33 and 2.34, we used the RWA, assuming $\delta \ll \omega_A$. This is the case, for example, for the force exerted on the atom by lasers used for cooling which are not too far red-detuned. For a CO_2 trap of ^{87}Rb atoms this assumption is not true. In that case $\omega_A \sim 2.5 \times 10^{15}$ and $\omega_{co_2} \sim 2.3 \times 10^{13}$ then $\delta \sim 2.4 \times 10^{15} \sim \omega_A$. Therefore the RWA is not applicable here.

2.3.1 The Far Detuned Limit

We consider the *far-detuned* case in which $\delta \ll \omega_A$, and $\delta \gg \Gamma$. The treatment in this section follows that in [5]. First we'll describe the classical oscillator model. When the atom is placed into the laser light, the electric field $\mathbf{E}(\mathbf{r},t) = \hat{\mathbf{e}}\tilde{E}(\mathbf{r})\, e^{-i\omega t} + c.c.$ (which oscillates at a frequency ω_L) induces an atomic dipole moment $\mathbf{p} = \hat{\mathbf{e}}\tilde{p}(\mathbf{r})\, e^{-i\omega t} + c.c.$ that oscillates at the driving field frequency. The interaction potential of the induced dipole moment in the driving field is

$$U(\mathbf{r}) = -\frac{1}{2}\langle \mathbf{pE}\rangle = -\frac{1}{2\epsilon_0 c} Re\left(\alpha\left(\omega_L\right)\right) I(\mathbf{r}) \tag{2.35}$$

where α is the complex polarizability of the atom, defined through $\tilde{p} = \alpha\tilde{E}$ and it depends on the driving frequency ω_L. The field intensity at the location $\mathbf{r}$ is $I(\mathbf{r}) = 2\epsilon_0 c|\tilde{E}|^2$. The force is the gradient of this potential

$$\mathcal{F}_{dipole} = -\nabla U(\mathbf{r}) = \frac{1}{2\epsilon_0 c} Re(\alpha)\, \nabla I(\mathbf{r})\,. \tag{2.36}$$

The power absorbed by the dipole from the field (and then re-emitted as dipole radiation) is given by

$$P_{abs} = \langle \dot{\mathbf{p}}\mathbf{E}\rangle = 2\omega Im\left(\tilde{p}\tilde{E}^{*}\right) = \frac{\omega}{\epsilon_0 c} Im(\alpha)\, I$$

This absorption rate can be considered quantum mechanically as due to photon absorption and a subsequent spontaneous emission at the scattering rate

$$\Gamma_{sc}(\mathbf{r}) = \frac{P_{abs}}{\hbar\omega} = \frac{1}{\hbar\epsilon_0 c} Im(\alpha)\, I(\mathbf{r}) \tag{2.37}$$

The polarizability is calculated according to the Lorentz model in which the atom's electron which forms the dipole moment is treated as a classical oscillator. By integrating the equation of motion $\ddot{x} + \Gamma_\omega \dot{x} + \omega_A^2 x = -eE(t)/m_e$ one finds that

$$\alpha = \frac{e^2}{m_e}\frac{1}{\omega_A^2 - \omega^2 - i\omega\Gamma_\omega}$$

where

$$\Gamma_{\omega} = \frac{e^2\omega^2}{6\pi\epsilon_0 m_e c^3} \tag{2.38}$$

is the classical damping rate due to radiative energy loss. Defining $\Gamma \equiv \Gamma_{\omega_A} = \left(\omega_A/\omega\right)^2 \Gamma_{\omega}$, one obtains

$$\alpha = 6\pi\epsilon_0 c^3 \frac{\Gamma/\omega_A^2}{\omega_A^2 - \omega^2 - i\left(\omega^3/\omega_0^2\right)\Gamma} \tag{2.39}$$

In a semi-classical approach one may calculate the polarizability by considering a two-level quantum mechanical atom interacting with a classical radiation field. In this approximation , when saturation effects can be neglected, this semi-classical approach yields exactly the same result as Eq. 2.39 for the polarizability with only one modification. The damping rate Γ is determined by the dipole matrix element between the ground and the excited state

$$\Gamma = \frac{\omega_A^2}{3\pi\epsilon_0 \hbar c^3} |\langle e|\mu|g\rangle|^2 \tag{2.40}$$

We should note here that Eq. 2.39, is valid only when saturation effects are negligible. However, for the laser intensities and detuning of a CO_2 dipole trap, the saturation is very low. From the above results (Eq. 2.37, Eq. 2.39) one finds that in the large detunings and negligible saturation

$$U\left(\mathbf{r}\right) = -\frac{3\pi c^2}{2\omega_A^3}\left(\frac{\Gamma}{\omega_A - \omega} + \frac{\Gamma}{\omega_A + \omega}\right) I\left(\mathbf{r}\right) \tag{2.41}$$

$$\Gamma_{sc}\left(\mathbf{r}\right) = \frac{3\pi c^2}{2\hbar\omega_A^3}\left(\frac{\omega}{\omega_A}\right)^3\left(\frac{\Gamma}{\omega_A - \omega} + \frac{\Gamma}{\omega_A + \omega}\right)^2 I\left(\mathbf{r}\right) \tag{2.42}$$

where we assumed that $\delta \gg \Gamma$. Typically, the condition $\delta \ll \omega_A$ also holds. Then the counter rotating term in Eqs. 2.41 and 2.42 is neglected in the RWA. In this case, the expressions for the dipole potential and the scattering rate reduces to

$$U\left(\mathbf{r}\right) = \frac{3\pi c^2}{2\omega_A^3}\frac{\Gamma}{\delta} I\left(\mathbf{r}\right) \tag{2.43}$$

$$\Gamma_{sc}\left(\mathbf{r}\right) = \frac{3\pi c^2}{2\hbar\omega_A^3}\left(\frac{\Gamma}{\delta}\right)^2 I\left(\mathbf{r}\right) \tag{2.44}$$

and then

$$\hbar\Gamma_{sc}\left(\mathbf{r}\right) = \frac{\Gamma}{\delta}U\left(\mathbf{r}\right) \tag{2.45}$$

It is evident that the scattering rate can be reduced while maintaining the trap depth by increasing the intensity and increasing the detuning $|\delta|$, since the dipole potential scales as I/δ, and the scattering rate scales as I/δ^2.

2.3.2 The Quasi-electrostatic Limit (QUEST)

A QUEST is a dipole trap considered in the *quasi-electrostatic limit*, in which the laser frequency is far below any atomic dipole resonance. In the case of a CO_2 trap of Rb atoms, the condition $\delta \ll \omega_A$ does not hold, and Eqs. 2.43, 2.45 and 2.44 are no longer valid. In this regime the field is treated as quasi-static and the trapping potential of the trap is the first order DC Stark shift of the the ground state due to all of the dipole-allowed excited states. This kind of dipole trap was first suggested and implemented by Takekoshi et. al. [7, 6]. The treatment in this section follows that in [5]. In this limit the dipole potential is simply

$$U\left(\mathbf{r}\right) = -\alpha_{stat}\frac{I\left(\mathbf{r}\right)}{2\epsilon_0 c} \tag{2.46}$$

where α_{stats} denotes the static polarizability ($\omega = 0$). For the ground state of Rb, Eq. 2.41 is well approximated by setting $\omega \to 0$ to receive

$$U\left(\mathbf{r}\right) = -\frac{3\pi c^2}{\omega_A^3}\frac{\Gamma}{\omega_A}I\left(\mathbf{r}\right) \tag{2.47}$$

Using Eqs. 2.41 and 2.42, and the quasi-electrostatic limit one reaches the following relation between the scattering rate and the trapping potential

$$\hbar\Gamma_{sc}\left(\mathbf{r}\right) = 2\left(\frac{\omega}{\omega_A}\right)^3\frac{\Gamma}{\omega_A}U\left(\mathbf{r}\right) \tag{2.48}$$

This result produces a scattering rate of less than $2 \times 10^{-3}Hz$ for a CO_2 trap of ^{87}Rb atoms. Therefore the photon scattering rate can be safely neglected and the

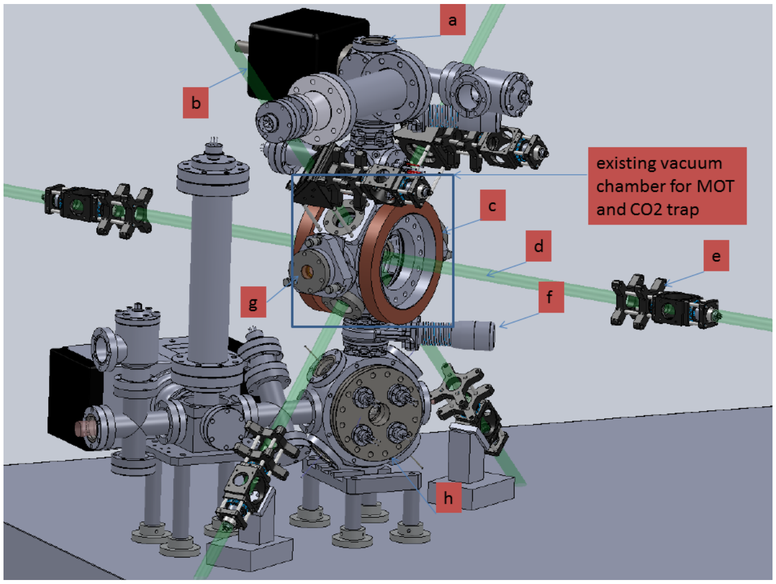

Fig. 1: A CAD drawing of the complete atom-ion experiment. The main chamber was used to trap atoms in a MOT and then load them to a focused CO_2 laser beam which formed the dipole trap. (a) YAG standing wave escalator port. Another port will be under the ion chamber marked by - h. (b) vacuum ion pump for ultra-high vacuum in the upper MOT and dipole trap chamber. (c) MOT magnetic quadrupole field coils. (d) MOT beams. (e) MOT beam expanders. (f) gate valve for separation between the upper and lower chamber. (g) CO_2 laser beam port and adjustable intra-vacuum lens holder. (h) Ion Paul-trap vacuum chamber that will be attached to the upper chamber in the future.

potential is truly a conservative since virtually no radiation is lost to the vacuum (the reservoir).

3 Experimental Setup

The system consists of an ultra-high vacuum chamber in which neutral atoms are initially cooled to below $1mK$ and then loaded into a focused beam of a CO_2 laser. The focus of this beam is adjusted to overlap with the center of the MOT for optimized loading of the dipole trap. In the future, the setup is planned to consists of another vacuum chamber below the chamber for the neutral atoms, for cooling, trapping and manipulating of one or several ions in a Paul trap as shown in Fig.

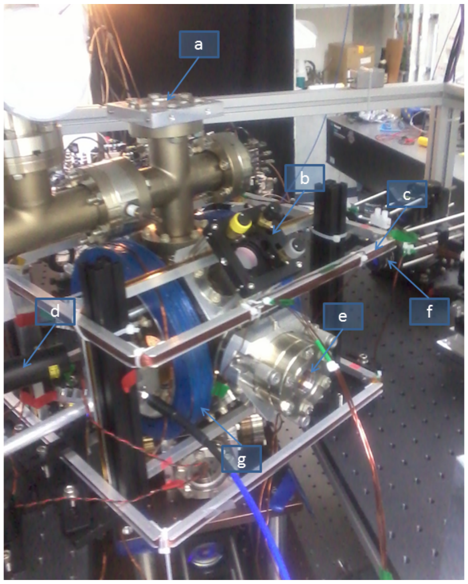

Fig. 2: A photograph of the vacuum chamber. (a) a port for the YAG standing wave escalator. (b) one of the retro reflecting mirror-$\lambda/4$ doublet. (c) magnetic field compensation coils (d) CCD camera for imaging of the MOT and dipole trap. (e) CO_2 beam exit port. (f) absorption beam aimed at the CCD camera through the center of the chamber. (g) magnetic field coils of the MOT

1. The trapped and cooled neutral atoms in the dipole trap will be transferred to the lower chamber, where ions will be trapped, via an optical standing wave "escalator" generated by two vertical YAG laser counter-propagating beams with a controlled phase difference between them. Outside of the vacuum chamber, is pair of coils arranged in an anti-Helmholtz configuration to produce the necessary magnetic quadrupole field for MOT operation. In addition to these coils three more pairs of coils arranged in a Helmholtz configuration are used to compensate for stray magnetic fields in the MOT center. The procedure of canceling the stray field is described in Sec. 4.2.2.

3.1 Vacuum System

Our vacuum chamber is Kimball Physics 6″ Octagon Chamber. Inside are the

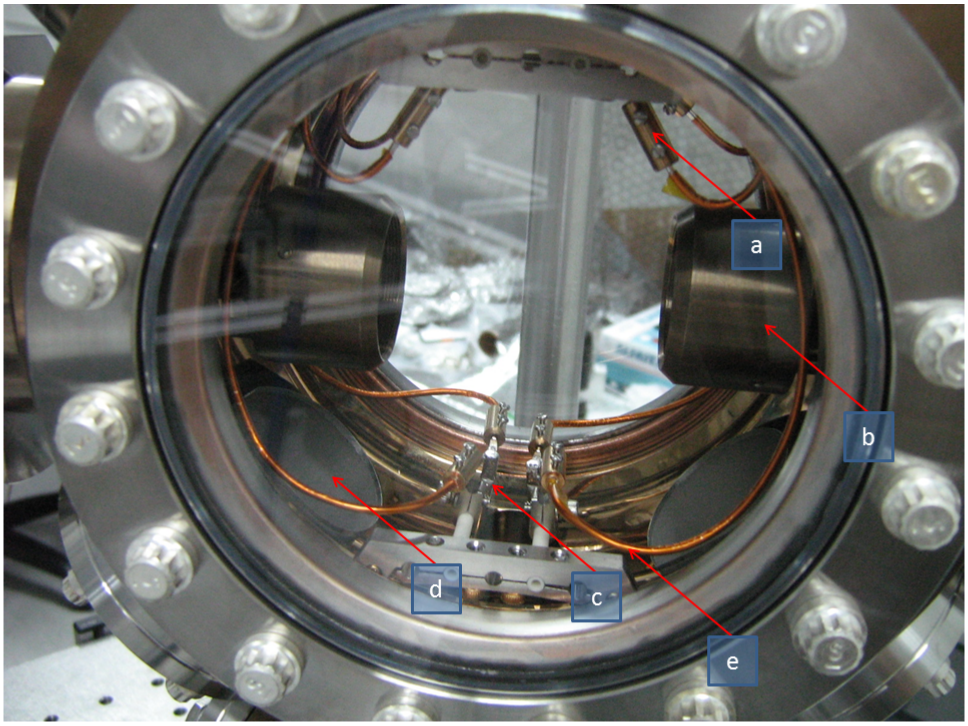

Fig. 3: A closeup of the vacuum chamber interior as seen through the main viewing ports. The focus of the CO_2 beam in which the dipole trap is formed is approximately in the middle between the two lenses held by the lens holder - (b). (a) and (e) wires to the Rb dispensers. (b) $ZnSe$ intra-vacuum lens holder. (c) Sr dispensers. (d) nonevaporable getter pump.

atom dispensers for both Rb[1] and of Sr[2], as can be seen in Fig. 3. Fused silica windows are installed on each of the chamber ports through which the lasers for trapping and imaging enter and exit the chamber. Imaging is performed through the large $6''$ window due to the large numerical aperture required. The ultra high vacuum in the chamber is achieved using a $20l/sec$ ion pump[3] (see Fig. 1) and nonevaporable getter (NEG) pumps installed inside the chamber (see Fig. 3).

---

[1] Alvasource

[2] home made

[3] Varian Vaclon 20 Plus StarCell

3.2 Magnetic Coils

The main pair of magnetic coils is arranged in an anti-Helmholtz configuration to produce a quadrupole magnetic field for the MOT. They are installed outside of the vacuum chamber as depicted in Fig. 1. With current of $4A$ we calculated a field gradient of $10G/cm$ at the trap center.

In addition to the MOT coils, three pairs of compensation coils were added to the system, each arranged in approximately a Helmholtz configuration with three orthogonal axes. Their purpose is to compensate for stray magnetic fields in the center of the vacuum chamber. The magnitude of the stray field was measured to be $\approx 0.3G$ and compensation was done with currents ranging between $30mA$ to $300mA$ in the compensation coils. Both the compensation coils and the MOT coils are shown in Fig. 2.

3.3 MOT Laser System

The MOT was composed of three beams, each retro-reflected using a mirror and a $\lambda/4$ plate attached to it, in order to obtain the counter propagating beam with an opposite circular polarization necessary for the MOT operation. The beams were generated using a tapered amplifier[4] with output power of $\sim 1W$ at a wavelength $780\,nm$. The tapered-amplifier light went through an acousto-optic modulator in a double-pass configuration [21], then it was coupled to three PM single mode fibers, each transported light to one of the retro-reflected beams. The acousto-optic double-pass served as a fast beam shutter and as a controller over the cooling light power and frequency. Each fiber's output power was measured to be $\approx 35mW$. The beams are expanded from the output coupler of the fibers using specially designed beam expanders which output a $20mm$ MOT beam diameter. A picture of the beam expander is shown in Fig. 5. The beam intensity was thus typically $\approx 11mW/cm^2 = 6.6I_{sat}$ [3]. The detuning during the MOT build-up phase was $-20MHz$

---

[4] model EYP-TPA-0780-01000-3006-CMT03-0000

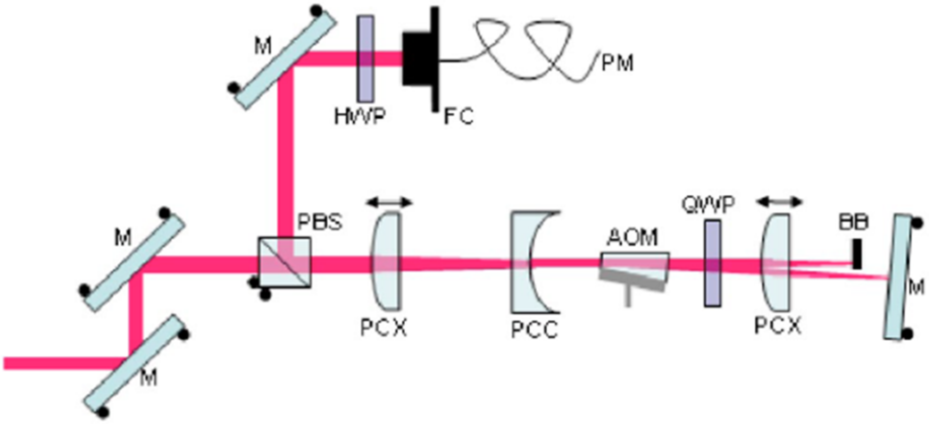

Fig. 4: Schematic drawing of the double-pass system. M: mirror. PBS: polarizing beam splitter. PCX: plano-convex lens. PCC: planoconcave lens. AOM: acousto-optic modulator. QWP: quarter-wave plate. BB: beam block. HWP: half wave plate. FC: fiber coupler. PM: polarization maintaining fiber. The circles that are attached to some of the optics represent angular adjustment knobs. The arrows above two of the lenses indicate that they are held in lens-focusing mounts. Figure was taken from [21]

3.3.1 Frequency Control

The tapered amplifier amplifies light from a DFB laser diode[5] which is offset locked to a stable reference laser. Using a frequency counter, implemented using a Field Programmable Gate Array (FPGA)[6] and a digital frequency divider, implemented using a commercial Phase-Lock Loop (PLL) evaluation board[7]. Using this offset locking the lock off-set between the lasers and therefore also the cooling beams frequency could be scanned in a range of $0 - 150 MHz$. The reference laser as

---

[5] model Eagleyard Photonics EYP-DFB-0780-00080-1500-TOC03-0002

[6] NI 7852R

[7] Analog Devices EVAL-ADF4113

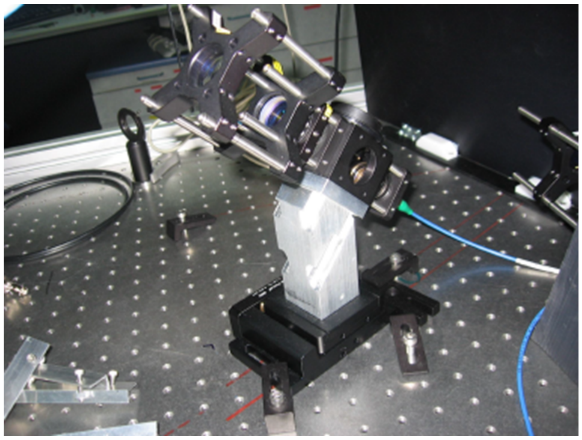

Fig. 5: Specially designed MOT beam expander. Consists of a PBS inside the cube in the middle followed by a $\lambda/4$ plate which produces the circular polarization and two lenses for expanding the beam to $\approx 20mm$.

well as the repump laser are locked to absorption lines in a Rb vapor cell using saturation absorption spectroscopy as illustrated in Fig. 6. A reference laser was locked to the crossover peak between the $F = 2 \rightarrow F' = 3$ and the $F = 2 \rightarrow F' = 2$ which is $133.25MHz$ red of the $F = 2 \rightarrow F' = 3$ (the cooling transition) [3]. A part of the reference beam is diverted to an AOM which shifts the frequency $133.25MHz$ to the red and into resonance with the $F = 2 \rightarrow F' = 2$ transition, to obtain a depumper beam for optical pumping of atoms from the $F = 2$ to the $F = 1$ dark state. The repump laser is locked to a second saturation absorption setup and is locked to the crossover peak $114MHz$ below the $F = 1 \rightarrow F' = 2$ transition. It is brought to resonance by an AOM shifting the beam frequency to the blue by $114MHz$. The DFB lasers' frequency is sensitive to both temperature and current. In order to control their temperature each of the three DFB lasers is thermally coupled to an Aluminum block attached to the table and used as a heat sink. The temperature is controlled using a thermo-electric cooler (TEC) which transfers heat from the DFB diode to the heat sink. Both the current and the temperature are controlled by a designated controller for each DFB laser. The typical temperature set point for the DFB lasers is around $9°C$ therefore the lasers are encapsulated in a PVC box in nitrogen atmosphere in order to prevent water condensation on the diode.

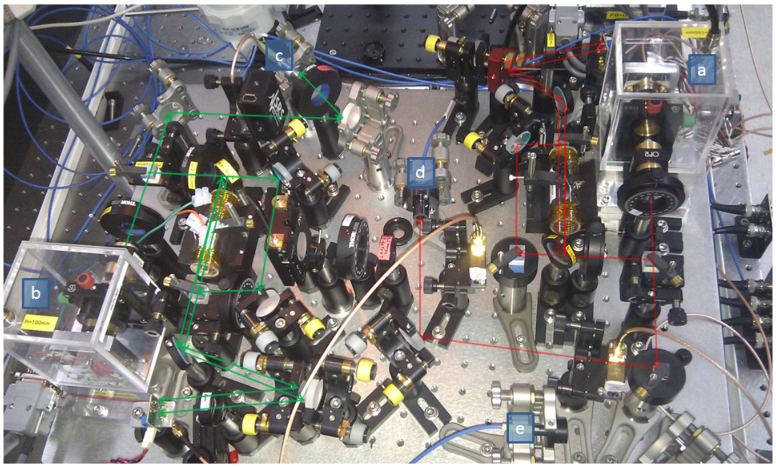

Fig. 6: An image of the saturation absorption spectroscopy setup of the reference and repump lasers. The red arrows represent the beam path for the reference laser (a). The green arrows represent the beam path of an identical configuration for the repump laser (b). (c) the repump fiber. It goes directly to the atoms. (d) "depumper" fiber directly to the atoms. (e) fiber to offset locking system

The locking was programmed to the NI FPGA card using NI Labview interface. We used a Matlab code which linked Matlab with the Labview interface, based on an implementation made by our group colleagues in the trapped ions lab. Thus we could control the detuning and power of the MOT beams (as well as other experimental parameters) using Matlab scripts in a most simple manner.

3.4 CO_2 Laser System

The dipole trap is made of a single beam generated by an industrial $80W$ CO_2 laser[8], focused in the center of the vacuum chamber and overlapping the MOT. The beam line is illustrated in Fig. 8 We used the maximal output power of the laser throughout the experiment to avoid temperature fluctuations which induce power instability. The beam power entering the vacuum chamber is controlled

---

[8] model: Coherent C55L

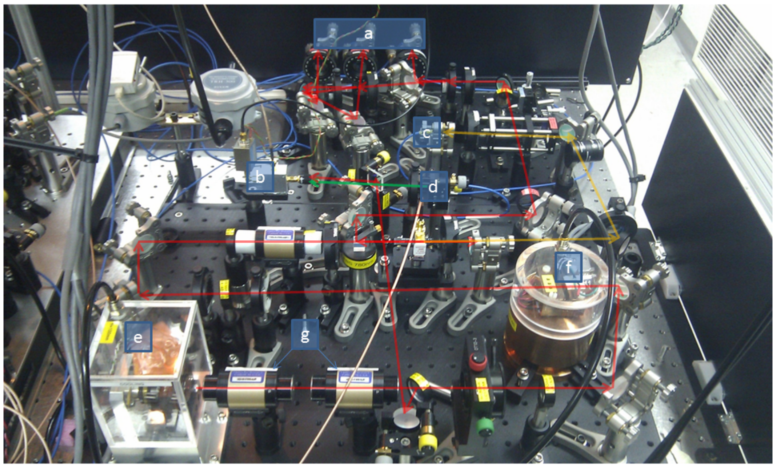

Fig. 7: An image of the offset locking system. The AOM in the middle is part of the double-pass configuration. (a) fibers for the cooling beams. (b) photodiode measuring the beat-note between the master (reference) laser and the slave. (c) fiber to the double-pass configuration of the absorption beam. (d) fiber from the master (reference) laser. (e) the slave laser providing the input for the tapered amplifier. (f) the tapered amplifier (g) optical isolators.

by a water cooled acousto-optic modulator[9] (AOM) which provides both as an analog controller and as a fast switch (rise/fall time is $\approx 0.5\mu sec$). This beam is the 1th diffraction order of the AOM's output and its power is determined by the RF power operating the AOM. The beam is focused by a $31.8mm$ @ $\lambda = 10.6\mu m$ aspherical lens inside the vacuum chamber. Its position relative to the chamber's center is adjustable using a specially designed lens holder. Another lens opposite to the focusing lens is used to collimate the beam back and make sure the beam power is getting out of the chamber through the exit port of the chamber. The output beam power is measured. The waist of the trap is determined by the width of the beam w_{lens} on the aspherical lens according to the approximation $w_0 \approx \frac{\lambda f}{\pi w_{lens}}$ which is valid for $z_R \gg f$ where z_R is the Rayleigh range before the lens and f is the lens' focus. The width of the beam on the aspherical lens is

---

[9] Gooch and Housego 37027-5

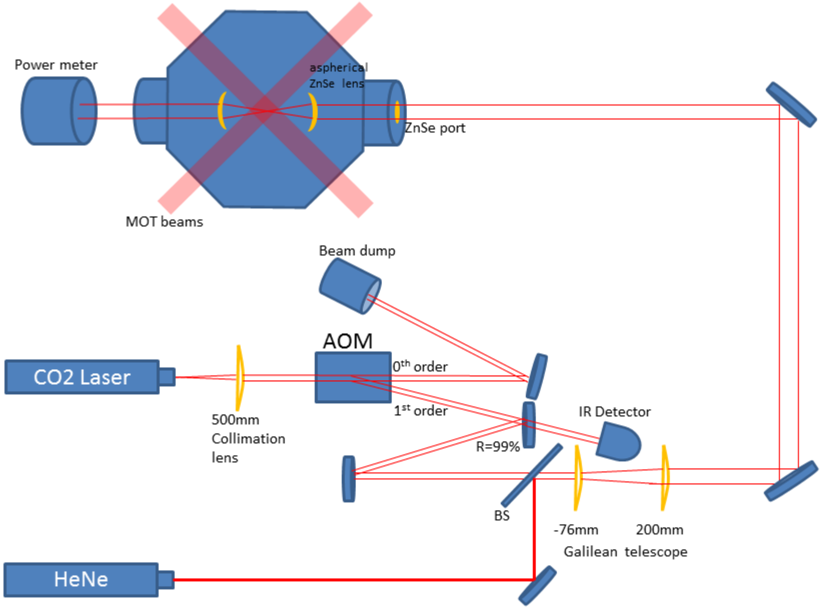

Fig. 8: A diagram of the beam line of the CO_2 laser producing the dipole trap. The acousto-optic modulator (AOM) is used as an analog power controller and a fast shutter. The IR detector is a fast photo diode suitable for the CO_2 laser wavelength as part of a future closed loop for control over the beam power. The $HeNe$ laser proved to be a very helpful tool for beam alignment due to its beam visibility. The Galilean telescope was used to adjust the beam width on$ZnSe$ port and thus control the waist of the dipole trap. The power of the beam was measured after the exit port of the vacuum chamber. All of the lenses are $ZnSe$ and are AR coated.

controlled by a Galilean telescope more than $1m$ away from the chamber entrance port.

3.5 Imaging

3.5.1 Fluorescence Imaging

Some of our measurements were performed by collecting scattered photons from the atoms in the MOT and imaging these photons on a CCD camera. The imaging occurs while the MOT beams are turned on and the atoms scatter light in all directions at a given rate by Eq. 2.31

$$N_{ph} = N_{at}\frac{\Gamma}{2}\frac{s_0}{1+s_0+4\left(\frac{\delta}{\Gamma}\right)^2}t_{exp}$$

where t_{exp} is the exposure time of the CCD, N_{at} is the number of atoms in the MOT. The number of photons detected by the CCD is $N_c = \eta N_{ph} d\Omega$ where $d\Omega$ is the solid angle that our imaging optics covers and η is the CCD quantum efficiency. The atom number is then

$$N_{at} = \frac{N_c}{t_{exp}\eta d\Omega}\frac{2}{\Gamma}\frac{1+s_0+4\left(\frac{\delta}{\Gamma}\right)^2}{s_0}$$

A similar result is obtained by imaging onto a photo-multiplier tube (PMT),

$$N_{at} = \frac{i_{PMT}}{Me\eta d\Omega}\frac{2}{\Gamma}\frac{1+s_0+4\left(\frac{\delta}{\Gamma}\right)^2}{s_0} \tag{3.1}$$

where i_{PMT} is the current signal from the PMT, M is the multiplication factor of the PMT (the number of electrons out of the cathode per electron out of the anode) and η is the quantum efficiency of the PMT.

3.5.2 Absorption Imaging

Most of the measurements on the trapped atoms both in the MOT as well as in the dipole trap were done by absorption imaging. The absorption beam is resonant with the $F = 2 \rightarrow F' = 3$ transition. It is derived from the amplified light in the offset locking system (see Fig. 7) after which it passes through an acousto-optic in a double-pass configuration as shown in Fig 4. The double pass system allows to scan the beam frequency without changing the beam deflection angle thus not destroying the coupling to the sigle-mode fiber at the output of the double-pass [21]. The atoms are imaged to a CCD double shutter camera [10]. When the absorption beam intensity is small such that saturation effects can be

---

[10] PCO Pixelfly QE

neglected, the intensity passing through the atomic cloud follows Beer's law [22]

$$\frac{dI}{dz} = -n\sigma_0 I \tag{3.2}$$

where n is the cloud density and σ_0 is the photon scattering cross section. The intensity profile is then given by

$$I(x,y) = e^{-\tilde{n}\sigma_0}$$

where $\tilde{n}$ is the integrated, or column, density. When considering background stray light the image profile is

$$S(x,y) = S_0(x,y)\, e^{-\tilde{n}\sigma_0} + S_{bg}(x,y)\,.$$

Here $S_{bg}(x,y)$ is the contribution of the background to the image and is not associated with the absorption beam. In order to find out the column density and thus the number of atoms, two more images must be taken. One is an image of the absorption with the atoms in a dark state - $S_0(x,y)$ and another one imaging only the background with the absorption beam shut-off - $S_{bg}(x,y)$. From the three images one may obtain the transmission profile

$$\tilde{T} = \frac{S(x,y) - S_{bg}(x,y)}{S_0(x,y) - S_{bg}(x,y)} \tag{3.3}$$

From this result the column density is obtained by $\tilde{n} = -\ln\left(\tilde{T}\right)/\sigma_0$. The atom number is then given by

$$N = -\frac{A}{\sigma_0}\sum_{pixels} \ln\left(\tilde{T}\right) \tag{3.4}$$

where A is the pixel size divided by the image magnification.

3.6 RF Spectroscopy

We used an antenna, impedance matched to the fused silica port of the vacuum chamber to produce an RF oscillating magnetic field inside the vacuum chamber at a frequency of $f_{RF} = 6.8GHz$, the hyperfine splitting of the ground state of

^{87}Rb. The oscillating field introduces coupling between the m_F-sublevels of the ground state hyperfine manifold. The frequency was generated by an Anritsu signal generator supplying the desired frequency with a resolution of $1Hz$. Accuracy and stability of the Anritsu where derived from locking of its time base to a commercial Rb atomic clock (SRS). The signal generator output was further amplified by an RF amplifier n order to supply the necessary power for efficient coupling.

4 The MOT

The *magneto-optical trap* (MOT), is the trap from which the atoms are loaded to the CO_2 dipole trap. This kind of trap was first introduced in 1987 as described in [8]. It is necessary since the typical dipole trap depths are in the order of $\sim 1mK$, therefore most room temperature atoms will not be trapped in such a dipole trap and cooling the atoms to below this temperature is necessary. In addition, in order to achieve large atom ensembles the density of the atoms in the volume overlapping the dipole trap should be as large as possible. The MOT provides both the trapping (and hence large densities) and cooling mechanisms to achieve this goal. For ^{87}Rb, MOT operation relies on affordable standard diode lasers.

4.1 Operation Principles

The MOT consists of six beams that are red detuned from the atomic resonance. The beams are divided to three counter propagating pairs with opposite circular polarizations (each beam has right circular polarization looking towards it's **k**-vector). The propagation direction of each pair is orthogonal to that of the other two pairs to form trapping and cooling in three dimensions. It is instructive to describe a 1D MOT in order to explain the basic operation principles. In this scheme two counter propagating beams of opposite circular polarization drive a $J = 0 \rightarrow J' = 1$ transition with a slight detuning from resonance to the red. In addition, two coils with counter rotating currents, produce a quadrupole magnetic field with its node overlapping the intersection of the beams. The magnetic field

Fig. 9: A representative fluorescence image of the MOT. The CCD camera images the photons (wavelength of $780nm$) scattered by the atoms in the presence of the MOT beams.

induces a Zeeman shift of the sublevels of the $J' = 1$ level, $m_J = -1, 0, 1$. This shift causes an atom that is displaced from the trap center to scatter light more frequently from the beam directed back to the center, giving rise to a net radiative force towards the magnetic field null. In the limit of low laser intensity ($I \ll I_{sat}$), the force acting on the atom is the sum of the individual forces from the two beams according to Eq. 2.32 and accounting for the Zeeman shift $\pm\beta z$ in the detuning for the $\sigma^{\pm}$ beams respectively,

$$\mathcal{F}(z,v) = \hbar k \frac{\Gamma}{2} \left(\frac{s_0}{1 + s_0 + 4\left(\frac{\delta - (kv + \beta z)}{\Gamma}\right)^2} + \frac{s_0}{1 + s_0 + 4\left(\frac{\delta + (kv + \beta z)}{\Gamma}\right)^2} \right) \tag{4.1}$$

In the limit of small velocities ($|\mathbf{k} \cdot \mathbf{v}| \ll \Gamma$), the force can be approximated by

$$\mathcal{F}(z,v) = \hbar k \frac{4 s_0 \left(2\delta/\Gamma\right)\left(kv + \beta z\right)}{\left(1 + s_0 + \left(2\delta/\Gamma\right)^2\right)^2} \tag{4.2}$$

This force is modeled by a damped harmonic oscillator. Typically the trap frequencies are a few KHz while the damping rates are a few hundreds of KHz, therefore the oscillations are over-damped.

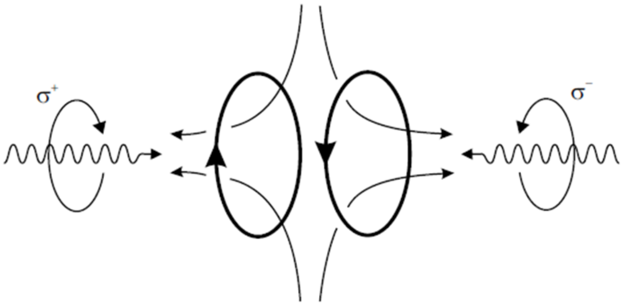

Fig. 10: A diagram of the MOT quadrupole magnetic field produced by two coils in an anti Helmholtz configuration and the two counter propagating beams with opposite circular polarizations $\sigma^+$and σ^-

The 1D scheme can be extended to three dimension by adding two more pairs of beams. For multilevel atoms the situation is more complex but the basic principles of operation are the same. The D_2 transition of ${}^{87}Rb$ relevant to the MOT operation is presented in Fig 12. The lasers drive the $5^2S_{1/2}$, $F=2 \rightarrow 5^2P_{3/2}$, $F'=3$ transition. Atoms scattering from the σ^+ beam, mainly induce a $m_F = 2 \rightarrow m_{F'} = 3$ transition [3]. This transition forms a closed cycle since the $F'=3$ level decays only to the $F=2$ level. However some population leaks to the $F=1$ ground state through off-resonance excitation of the $F'=2$ state which decays both to the $F=1$ and to the $F=2$ states. An atom in the $F=1$ state becomes dark and is no longer cooled nor trapped because of the large level separation of $\sim 6.8GHz$ between the $F=1$and the $F=2$ levels which takes the atoms far off resonance. Therefore an optical pumping laser (the *repump* laser) driving the $F=1 \rightarrow F'=2$ transition is needed, otherwise the atoms will be optically pumped to the dark state.

In order to achieve large numbers of trapped atoms in the MOT, one has to make the MOT beams as wide as possible while maintaining the intensity few

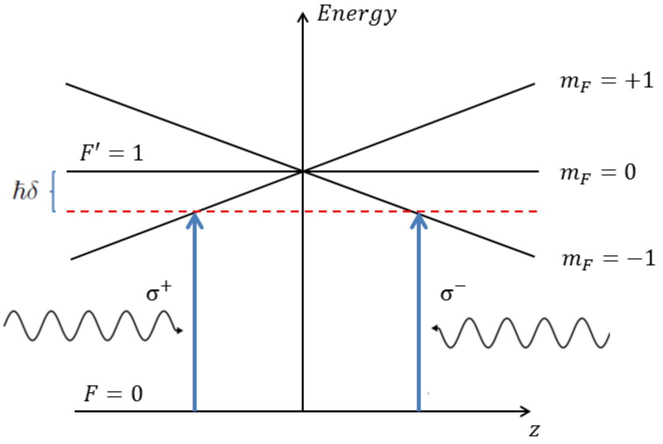

Fig. 11: The level structure of an atom in the 1D MOT scheme. The magnetic field inducing the Zeeman shift is linear in position and is null in the trap center. The $m_F = -1$ state is Zeeman shifted towards resonance with the beam of σ^- polarization which transfers momentum left towards the trap center. The $m_F = +1$ is shifted towards resonance with the σ+beam which transfers momentum right towards the trap center.

times larger than the saturation intensity. The dependence of the MOT size and density on the MOT parameters is described in [10].

As said above, for the loading of a dipole trap, one would like to have the highest density achievable of atoms with a temperature below $1mK$. However, the density in a MOT is limited since reabsorption of scattered photons from neighboring atoms and inelastic collisions have a significant effect in densities of $\sim 10^{11} atoms/cm^3$ which limits the atom density [11]. This problem can be somewhat compensated for by changing the parameters of the MOT after its loading to achieve temporarily atom density increase up to $10^{12} atoms/cm^3$ at the MOT center [12]. We investigated the number of atoms loaded to the CO_2 dipole trap as a function of these parameters and witnessed a strong dependence on some of

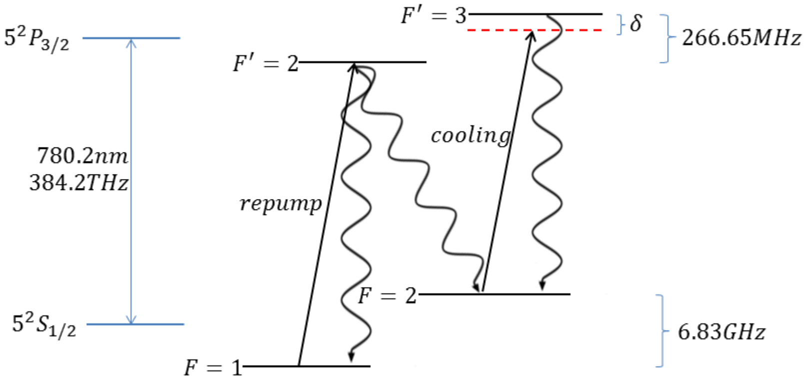

Fig. 12: The level structure of ^{87}Rb relevant for the operation of the MOT. The solid arrows represent the repump and cooling lasers and the wavy arrows represent spontaneous emission processes. The repump transfers the population leaking from the cycling transition $F = 2 \rightarrow F' = 3$ back to the $F = 1$ level.

them. More on that in Sec. 5.

4.2 MOT Characterization

4.2.1 MOT Dynamics

The dynamics of a typical MOT can modeled by a simple rate equation model governed by the equation [13]

$$\dot{N} = R - \Gamma N. \tag{4.3}$$

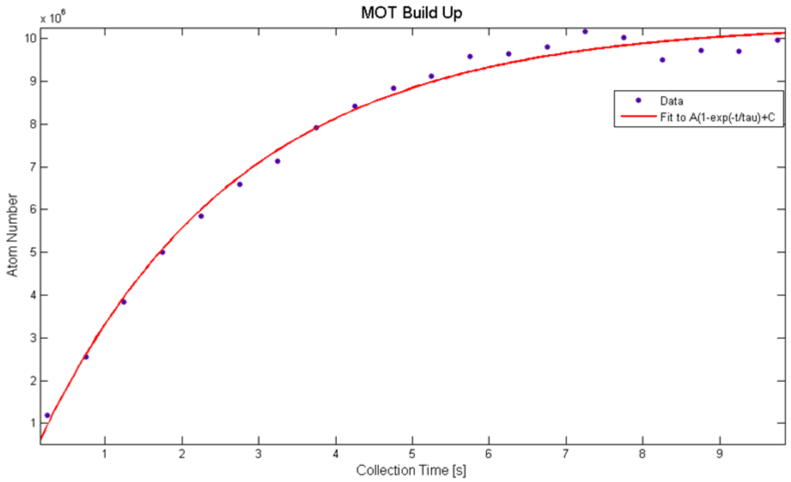

Fig. 13: MOT build up. $\tau_{buildup} = 2.6 \pm 0.3 sec$

Here R is the loading rate and $\Gamma = \frac{1}{\tau}$ is the loss rate from the MOT. Taking into account two-body collisions of an atom with the MOT and a thermal atom in the chamber only. Assuming $N(0) = 0$, the solution to this equation is

$$N(t) = N_s \left(1 - e^{-\Gamma t}\right) \tag{4.4}$$

where $N_s = \frac{R}{\Gamma}$ is the steady state solution to Eq. 4.3. The number of atoms in our MOT as a function of the loading time is shown in 13 A typical atom number in our MOT was 10^7 atoms after $2.5 sec$ of loading. We were able to increase the number of atoms by a factor of 5, by illuminating the chamber with UV light using a set of LEDs attached to the chamber. However the loading time has not changed. The loading rate is proportional to the ^{87}Rb partial pressure in the chamber $R = \kappa P_{Rb}$ while the loss rate Γ is proportional to the total pressure in the chamber $\Gamma = \alpha \left(P_{Rb} + P_{junk}\right)$ where P_{junk} is the pressure produced by all particles except ^{87}Rb with velocity small enough to be captured. Then the steady

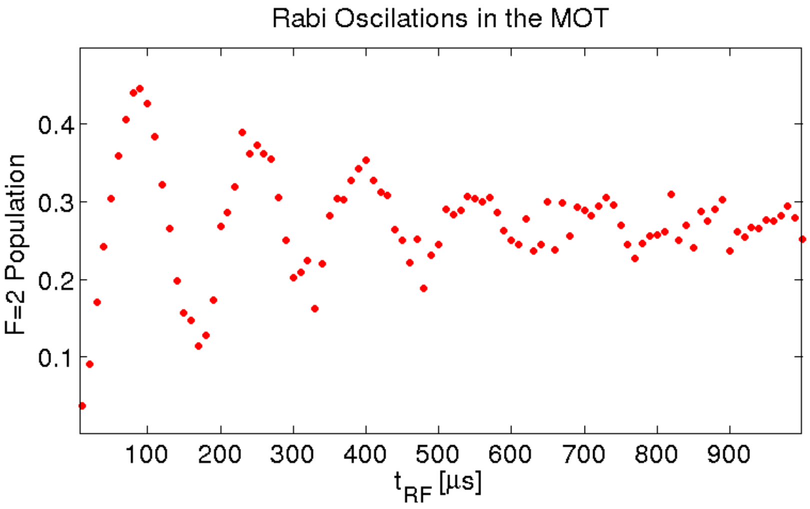

Fig. 14: Rabi oscillations of atoms in the MOT. Atoms initially are optically pumped to the $F = 1$ state. π-time is $\tau_\pi \approx 90\mu sec$.

state solution can be written as [14]

$$N_s = R\tau = \frac{\kappa}{\alpha}\frac{\frac{P_{Rb}}{P_{junc}}}{\left(\frac{P_{Rb}}{P_{junc}}+1\right)} \tag{4.5}$$

The partial pressure of the Rb atoms could be controlled by controlling the current flowing through the Rb getters. Therefore if the pressure is dominated by junk the steady state atom number is linear with the Rb pressure and the build-up time τ does not change. Otherwise if the pressure is dominated by Rb the loss rate Γ changes linearly with the Rb pressure and the steady state atom number tends to a constant depending on other MOT parameters. We have not seen a dependence of the build-up time on the Rb pressure when we increased the current through the Rb getters, therefore we concluded that the pressure is not Rb dominated. In addition, comparing our MOT size of $\sim 10^7$ to MOT sizes in other groups with a similar setup [18, 16] of 10^9 atoms, our MOT is very small.

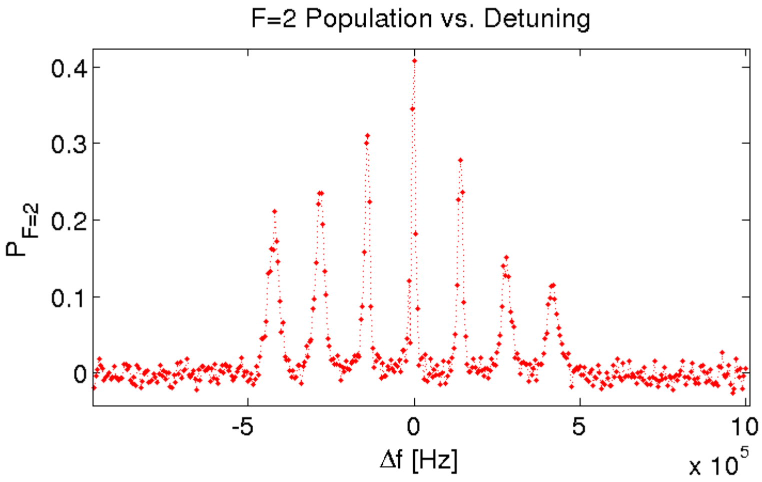

Fig. 15: The $F = 2$ population after a $85\mu sec$ π-pulse corresponding to the clock transition @$6.8GHz$ ($\Delta f = 0$) as a function of the detuning. Initially the atoms were in the $F = 1$ state after optical pumping with the "depumper" beam (resonant with the $F = 2 \to F' = 2$ transition). The detuning was scanned in order to measure the magnetic field in the MOT position. a magnetic field of $B_{stray} = 0.2 \pm 0.02G$ was measured.

4.2.2 RF Spectroscopy

The purpose of the RF spectroscopy of the MOT was to exactly measure the magnetic field, in order to eliminate it using the compensation coils, for better MOT performance. A Rabi frequency of $\Omega > 2\pi \times 25kHz$ with an input power of $1 - 2W$ was observed. Fig. 15 shows the $F = 2$ population after a π-pulse versus the detuning from the clock transition @$6.8GHz$. The magnetic field is determined by the frequency difference between adjacent peaks. The clock transition $|F = 1, m_F = 0\rangle \to |F = 2, m_F = 0\rangle$ is responsible for the central peak. The next peaks are the $m_F = 0 \to m'_F = \pm 1$ transitions and $m_F = \pm 1 \to m'_F = 0$ displaced $\pm 0.7MHz/G$ from the clock transition. Next peaks further are the $m_F = \pm 1 \to m'_F = \pm 1$, $\pm 1.4MHz/G$ from the clock transition. Finally the furthest peaks are the $m_F = \pm 1 \to m'_F = \pm 2$ transitions which are $\pm 2.1MHz/G$ away from the clock transition. The measurement in Fig. 15 yields a magnetic field of $B_{stray} = 0.2 \pm 0.02G$ (averaged over the atomic cloud physical extent). An attempt to eliminate the magnetic field is shown in Fig. 17, where the current on one of the compensation coils (compensating in some direction) was scanned

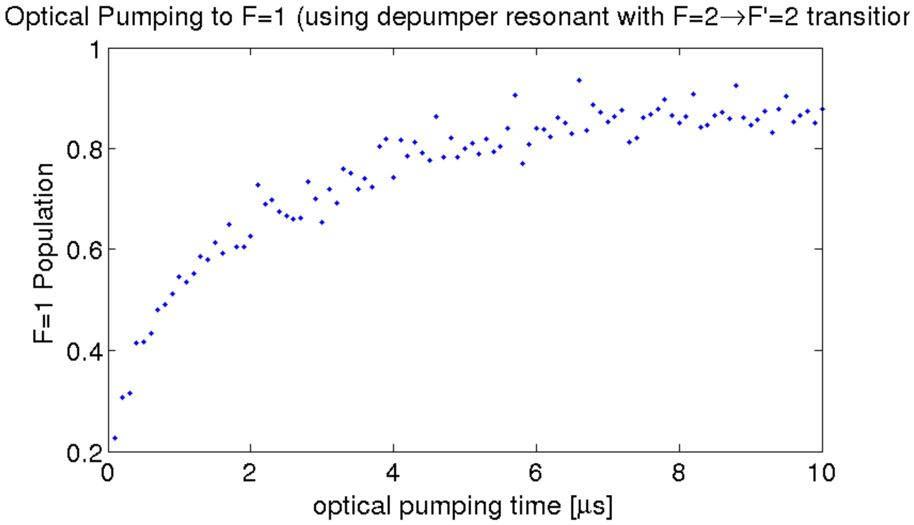

Fig. 16: Optical pumping time measurement of the atoms in the MOT. $\tau_p = 2.1 \pm 0.2 \mu sec$ from fit.

while the two other coils remained with a constant current. We started each measurement with an initial population of 0.9 either in the $F = 1$ or $F = 2$ state. This is done by optical pumping of the atoms with a beam resonant with either the $F = 2 \to F' = 2$ transition for initial population in the $F = 1$ state or the $F = 1 \to F' = 2$ transition for initially populating the $F = 2$ state.

5 The CO_2 Dipole Trap

5.1 Gaussian Beam Dipole Trap

The CO_2 laser beam has a Gaussian profile and the trap is obtained at the waist of the beam inside the vacuum chamber.The beam is focuesed using an intra-vacuum aspherical positive lens. The intensity profile of a Gaussian beam is given by

$$I(r,z) = \frac{2P}{\pi w^2(z)} e^{-2r^2/w^2(z)} \tag{5.1}$$

where z and r are the coordinates along and tangent to the optical axis respectively and P is the total beam power. $w(z)$ is the beam radius and is given by

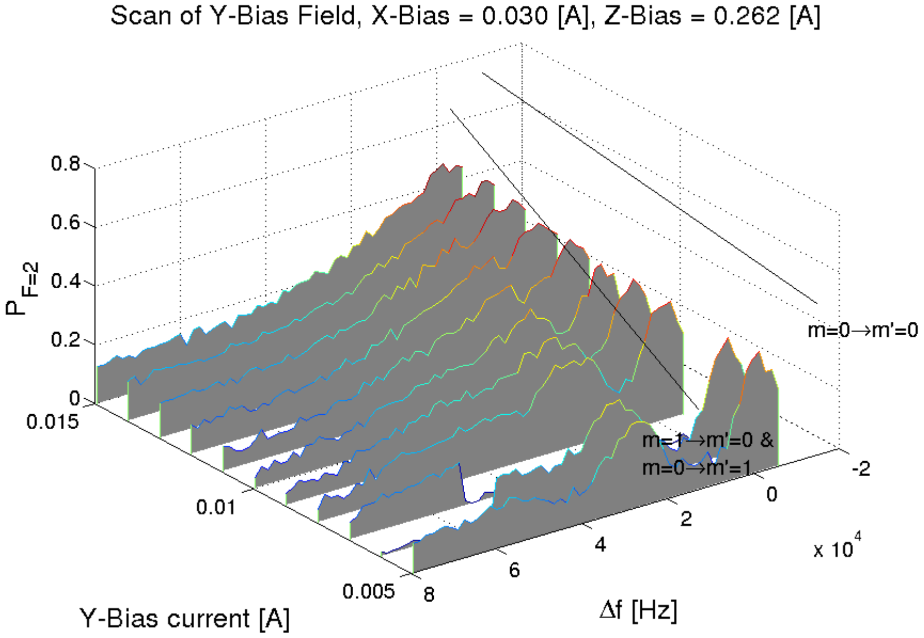

Fig. 17: The population of the $F = 2$ state after a π-pulse as a function of the RF detuning and the current in one of the magnetic compensation pair of coils. The central lobe represents the clock transition $m = 0 \rightarrow m' = 0$ which is insensitive to the magnetic field. The second lobe represents the $m = 1 \rightarrow m' = 0$ and the $m = 0 \rightarrow m' = 1$ transitions and it merges with the central lobe as the magnetic field diminishes.

$$w(z) = w_0\sqrt{1 + \left(\frac{z}{z_R}\right)^2}.$$

Here w_0 is the beam waist (the minimal radius of the beam which is located at $z = 0$) and z_R is called the *Rayleigh range*

$$z_R = \frac{\pi w_0^2}{\lambda} \tag{5.2}$$

λ is the wavelength. By substituting Eq. 5.1 in Eq. 2.46 the dipole potential created by a Gaussian beam of a CO_2 laser is

$$U(r, z) = -\frac{\alpha_{stat} P}{\pi\epsilon_0 c w^2(z)} e^{-2r^2/w^2(z)} \tag{5.3}$$

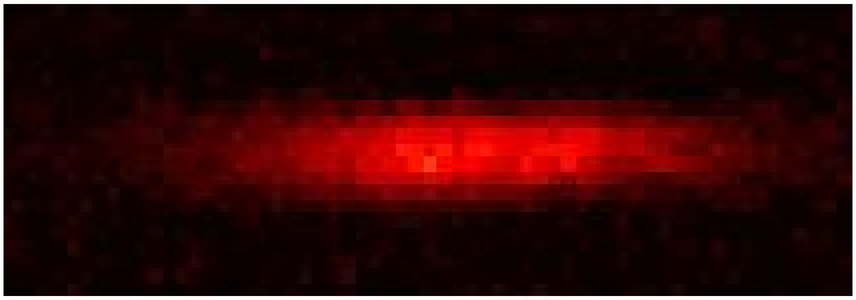

Fig. 18: A typpical absorption image of the dipole trap. The darker areas represent larger light intensity due to less shadow by the atoms.

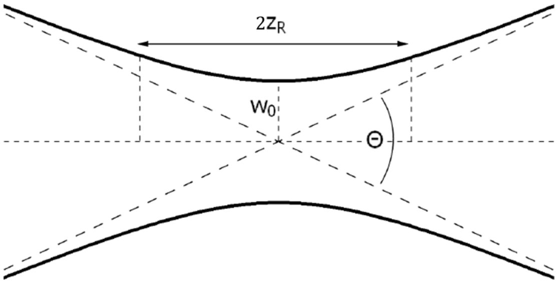

Fig. 19: An illustration of a Gaussian beam waist parameters.

There are two spring constants of the trap. The radial and the axial trap frequencies $\omega_r = \sqrt{\frac{1}{m}\frac{\partial^2 U}{\partial r^2}}$, and $\omega_z = \sqrt{\frac{1}{m}\frac{\partial^2 U}{\partial z^2}}$ respectively evaluated at $r, z = 0$. This results in

$$\omega_r = \sqrt{\frac{4U_0}{mw_0^2}}, \quad \omega_z = \sqrt{\frac{2U_0}{mz_R^2}} \tag{5.4}$$

where U_0 is the trap depth $U_0 = -U(0,0) = \frac{\alpha_{stat}P}{\pi\epsilon_0 c w_0^2}$. From knowing the radial frequency and the beam power one can determine the waist of the trap beam from $\omega_r = \sqrt{\frac{4\alpha_{stat}P}{m\pi\epsilon_0 c w_0^4}}$ which results in

$$w_0 = \left(\frac{4\alpha_{stat}P}{m\pi\epsilon_0 c\omega_r^2}\right)^{\frac{1}{4}} \tag{5.5}$$

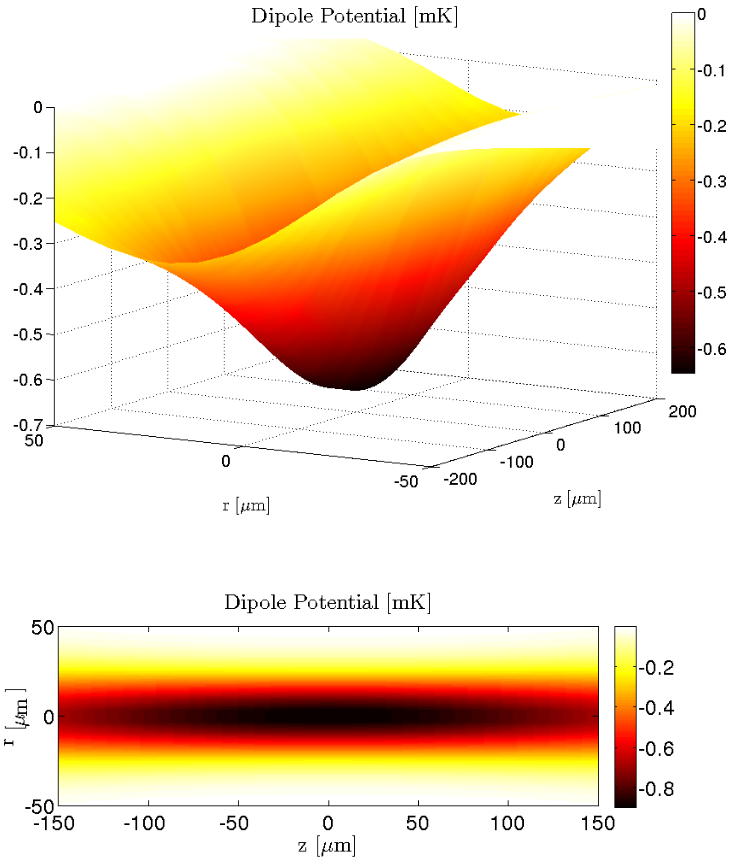

Fig. 20: A plot of the dipole potential for ^{87}Rb at a CO_2 laser beam waist. Plotted for $w_0 = 30\mu m$ and $P = 30W$. It evident that the spring constant in the radial (r-axis) direction is larger that that in the axial (z-axis) direction.

For a dipole trap with a beam waist of $w_0 = 30\mu m$, and optical power of $13W$ the potential depth is $U_0/K_B \approx 0.66mK$. The potential corresponding to such a beam is plotted in Fig. 20. For such a typical dipole potential the gravitational potential difference across a distance of w_0 is three orders of magnitude smaller than the potential depth therefore it can be neglected.

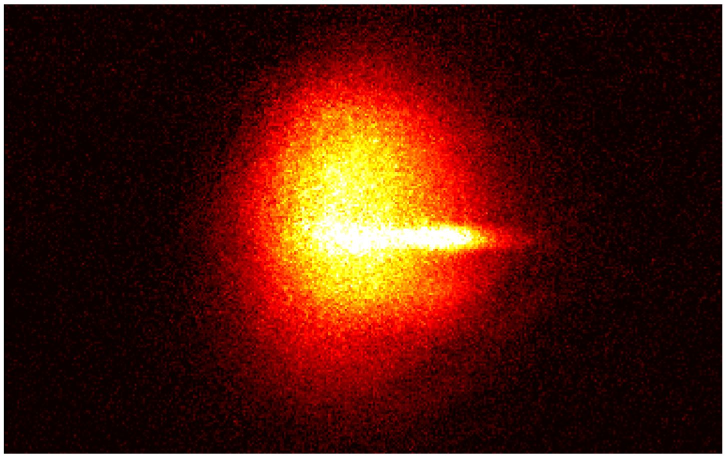

Fig. 21: A $\sim 0.5msec$ time of flight absorption image of the atoms. It is evident that the dipole trap (the cigar shaped cloud) is misaligned to the right of the MOT (the larger round cloud). Alignment in this stage is performed by iterations that eventually brings the dipole trap to the center of the MOT.

5.2 Loading and Alignment

In order to overlap the focus of the dipole trap with the MOT, we imaged the fluorescence from the MOT into a CCD placed far away form the chamber and on the CO_2 beam optical axis and moved the intra-vacuum ZnSe lens to bring the MOT to focus on the CCD center. The imaging was done through two irises positioned along the CO_2 laser beam line. After focusing is achieved the ZnSe lens was moved along the optical axis to compensate for the $3.16mm$ focal shift between the fluorescence wavelength at $780nm$ and the CO_2 laser wavelength at $10.6\mu m$. This method allowed enough atoms to be loaded into the dipole trap to get an initial signal. We then optimized the atom number in the CO_2 trap by gently moving the lens to take the focus closer to the MOT center.

We optimized the loading efficiency of the CO_2 trap by temporarily compressing the MOT. This is done by increasing the cooling beam detuning and reducing the repump intensity after the MOT [12]. After a MOT loading time of $5sec$, we scanned these MOT parameters and the compression duration after which the CO_2 trap was turned on. Then we measured the resulting temperature and number of atoms in CO_2 trap as a function of the scanned parameters to get a maximum number.

5.3 Characterization

5.3.1 Trap Frequencies Measurement

The CO_2 trap has two trap frequencies corresponding to the axial and radial spring constants as described in Sec. 5.1. In order to measure these frequencies we applied a $\sim 10\%$ modulation of the RF power to the CO_2 AOM. this way both of the spring constants of the dipole trap are modulated by the same frequency. Parametric heating of the atoms is expected with two resonances, at $2\pi f_{mod} = 2\omega_r$ and $2\pi f_{mod} = 2\omega_z$. Therefore for a fixed modulation time, we scanned the modulation frequency and counted the atoms in the trap immediately after the modulation and expected higher atom loss at the resonance frequencies due to the heating. Such a loss spectrum is shown in Fig. 22. As seen, a distinct resonance is observed at a frequency $f_{mod} \approx 6500Hz$ indicating that $\omega_r = 2\pi \times 3750Hz$. This measured frequency together with a beam power of $P = 18W$ in the chamber, indicate a waist of $w_0 = 29 \pm 3\mu m$ and trap depth of $\approx 1mK$ which is considerably larger than the atom's temperature. The error is estimated using an error of $1kHz$ (FWHM) of the resonance line. According to Eq. 5.4 the axial trap frequency is $\omega_z = \frac{\lambda}{\sqrt{2}\pi w_0}\omega_r \approx 2\pi \times 250Hz$.

We used another technique to measure the trap frequencies. The procedure is shutting the CO_2 power off during trap operation for a short period of time of $0.5msec$. The atomic cloud ballisticaly expands before the trap is turned on again. The spatial distribution subsequently oscillates at twice the trap frequency. We measure these oscillations by releasing the atoms from the trap at different times and performing time-of-flight measurements (see section 5.3.2). A representative measurement for which a parametric excitation measurement resulted in $\omega_r = 2\pi \times 7 \pm 2kHz$, is shown in Fig. 23 with the resulting trap frequency of $\omega_r = 2\pi \times 8.8 \pm 0.4kHz$. The two methods are thus seen to agree within the error margin.

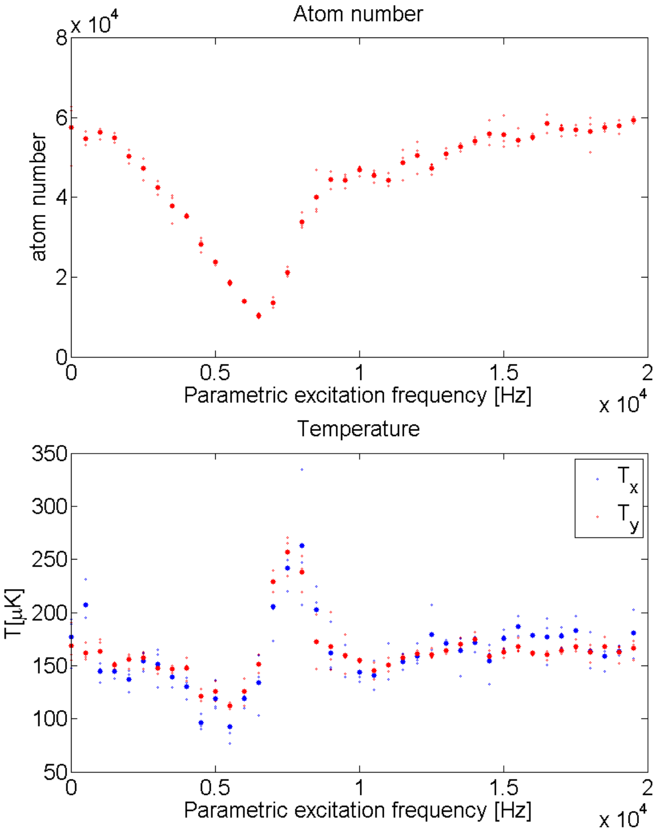

Fig. 22: In the upper plot, atom number after $250ms$ in a modulated beam power trap. The resonance is found at $\omega_{mod} \approx 2\pi \times 6500Hz$ corresponding with $w_0 = 29 \pm 3\mu m$. The temperature is shown in the lower plot with respect to the same modulation time. A significant temperature increase occurs above the resonance. The full dots represent the average of the empty dots which are repeated measurements at each frequency.

5.3.2 Trap Temperature and Atom Number

Since all of our measurements where done in time of flight (TOF - the time after the trapping is turned off abruptly), we evaluated the transmission $\tilde{T}$ (Eq. 3.3) by fitting the atomic cloud image to a two dimensional Gaussian in order to reduce the effect of the background noise in the atom number measurements. The temperature was measured by taking two TOF images at two different times. Assuming an initial Gaussian density profile with a spread of σ_0, at a later time t the density profile is Gaussian with a spread $\sigma_t^2 = \sigma_0^2 + \frac{k_B T}{m} t^2$ [23]. Thus the

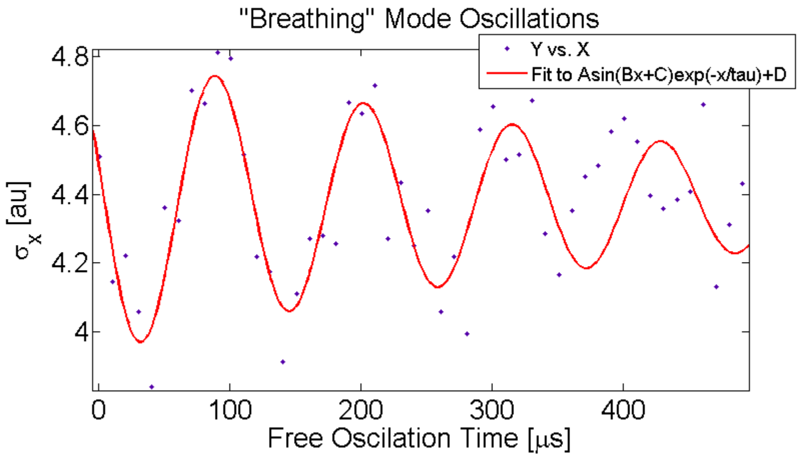

Fig. 23: The trap frequency according to the fit is $\omega_r = 2\pi \times 8.8 \pm 0.4kHz$. For the same waist and power the parametric excitation resulted in $\omega_r = 2\pi \times 7 \pm 2kHz.$.

temperature can be derived from,

$$T = \left(\sigma_t^2 - \sigma_0^2\right) \frac{m}{k_B t^2}. \tag{5.6}$$

The could's widthsσ_0 and σ_t, are derived from a Gaussian fit of the atomic cloud images. The time separation between images t is known. The trap life time is obtained from the slow decay rate of the atom number in the trap. According to the slower decay obtained from the fit in Fig. 25, the lifetime in the trap is $\tau_2 = 514 \pm 27msec$. The measurement started with 10^5 atoms in the trap which was a typical number throughout the experiment.

5.3.3 Phase-space Density and Collision Rate

Using the estimated trap waist, temperature and density profile the *phase-space density* and the *collision rate* of the atomic cloud can be derived. The following treatment is similar to that is [14]. The probability density $P(\mathbf{r}, \mathbf{p})$ of a particle in the trap to be in the state $(\mathbf{r}, \mathbf{p})$, assuming the particles do not interact is

$$P(\mathbf{r}, \mathbf{p}) = \frac{1}{\mathcal{Z}} e^{-\frac{\mathcal{H}(\mathbf{r}, \mathbf{p})}{k_B T}} \tag{5.7}$$

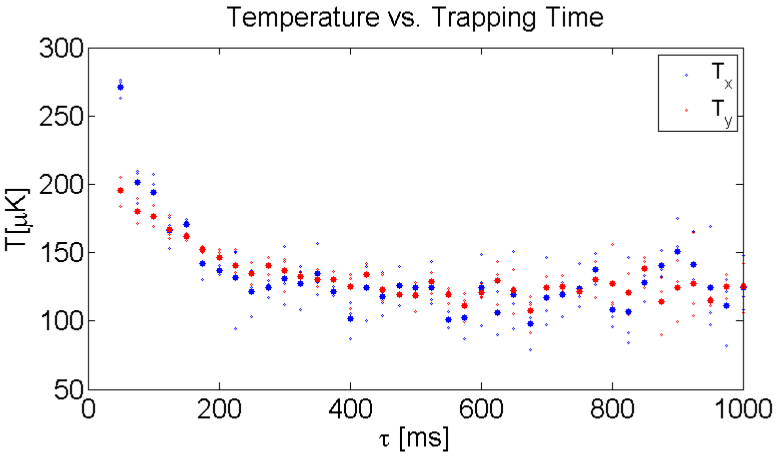

Fig. 24: The temperature as a function of time in two directions according to the spreads σ_x and σ_y of the Gaussian fit of the atomic cloud. Two different temperature for the x and y axes appear until a thermalization time of $\approx 150msec$ is reached. The full dots represent the average of the empty dots which are repeated measurements for each time.

where

$$\mathcal{H}\left(\mathbf{r},\mathbf{p}\right)=\frac{p^2}{2m}+\frac{1}{2}m\omega_x^2x^2+\frac{1}{2}m\omega_y^2y^2\frac{1}{2}m\omega_z^2z^2 \tag{5.8}$$

and $\mathcal{Z}$ is the partition function

$$\mathcal{Z}=\int d^3pd^3re^{-\frac{\mathcal{H}(\mathbf{r},\mathbf{p})}{k_BT}}=\frac{\left(2\pi k_BT\right)^3}{\omega_x\omega_y\omega_z} \tag{5.9}$$

The probability density to find a particle at the position $\mathbf{r}$ is obtained by integrating over its momentum

$$P\left(\mathbf{r}\right)=\frac{m^{3/2}\omega_x\omega_y\omega_z}{\left(2\pi k_BT\right)^{3/2}}e^{-\frac{1}{k_BT}\frac{m}{2}\left(\omega_x^2x^2+\omega_y^2y^2+\omega_z^2z^2\right)}. \tag{5.10}$$

According to the density distribution in the trap is

$$n\left(\mathbf{r}\right)=NP\left(\mathbf{r}\right) \tag{5.11}$$

where N is the total atom number in the trap. The average density is defined as $\bar{n}=\int d^3rP\left(\mathbf{r}\right)n\left(\mathbf{r}\right)=2^{-3/2}n_0$ where $n_0=N\frac{m^{3/2}\omega_x\omega_y\omega_z}{\left(2\pi k_BT\right)^{3/2}}$ is the peak density

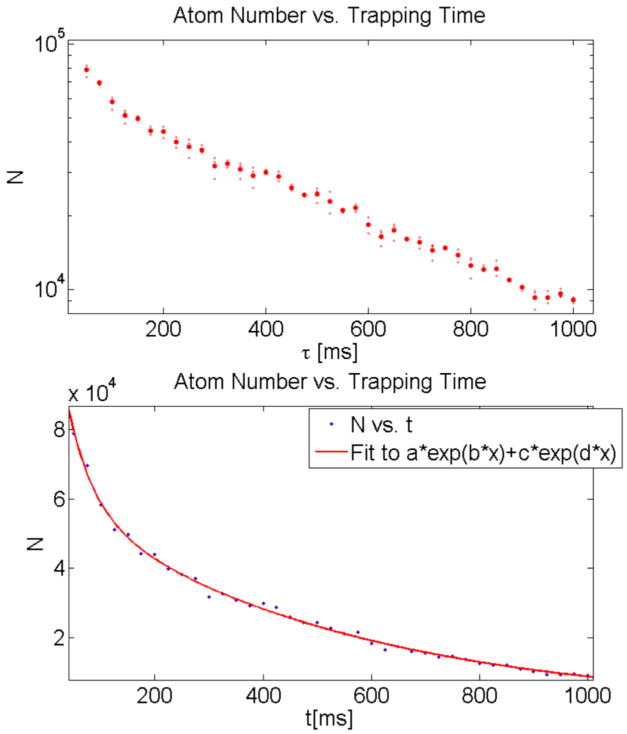

Fig. 25: (upper) Atom number as a function of trapping time on a semi-log scale for a waist of $w_0 \approx 29\mu m$ and beam power of $P = 18W$. Two exponential decay curves are observed. An initial decay curve with an exponential decay time of $\tau_1 = 47 \pm 15msec$ is due to evaporation of hot atoms from the trap. The slower decay curve of $\tau_2 = 514 \pm 27msec$ is due to collisions with background atoms. The two time scales are obtained using a two-decay-times fit (lower).

which is in the center of the Gaussian atomic cloud. We define also the effective volume $V = N/\bar{n} = 2^{3/2}\frac{(2\pi k_B T)^{3/2}}{m^{3/2}\omega_x\omega_y\omega_z}$. Accordingly we define an effective trap radius by $R = \left(\frac{3V}{4\pi}\right)^{1/3}$. The phase-space density is defined as

$$\rho(\mathbf{r}) = \lambda_{th}^3 n(\mathbf{r}) \tag{5.12}$$

where $\lambda_{th} = \frac{h}{\sqrt{2\pi m k_B T}}$ is the thermal de-Broglie wavelength. The peak phase-space density will be at the trap center and is given by

$$\rho_0 = N\frac{\hbar\omega_x\hbar\omega_y\hbar\omega_z}{(k_B T)^3}$$

In the case of a Gaussian trap the peak phase-space density at the center becomes $\rho_0 = N\frac{(\hbar\omega_r)^2\hbar\omega_z}{(k_BT)^3}$. For the representative values of $w_0 = 29\mu m$ waist and beam power of $P = 18W$ (corresponding to the measurement in Fig. 25) the peak phase-space density obtained after $150msec$ was $\rho_0 \approx 8 \times 10^{-6}$. The phase-space density remains similar (up to factor of 2) throughout the measurement. The collision rate can be obtained by the relation

$$\Gamma_{col} = \sigma_s \bar{n} v_{th} \tag{5.13}$$

where $\sigma_s = 5.4 \times 10^{-12} cm^2$ is the s-wave cross section of $Rb - Rb$ interaction and $v_{th} = \sqrt{\frac{3k_BT}{m}}$ is the thermal velocity. The collision rate corresponding to the measurement in Fig. 25 after $150ms$ is $\Gamma_{col} \approx 54Hz$.

5.3.4 Dependence on The Beam Waist

We measured the number of atoms and temperature, after a trapping time of $250msec$ and $18W$ beam power, as a function of the beam waist. The dependence is shown in Fig. 26 It is evident that the temperature drops and the atom number increases with increasing waist. The temperature decreases due to lower evaporation temperature of a shallower trap. The atom number increases due to larger trapping volume which covers more of the MOT during loading.

5.3.5 RF Spectroscopy

In addition to nulling the magnetic field using RF spectroscopy of the MOT, preliminary Rabi and Ramsey coherence times measurements of the atoms in the CO_2 trap were performed. In a Rabi measurement, the atoms are initially optically pumped to the $F = 1$ state and the populations are measured as a function of the RF pulse duration . The decay rate of the oscillations determines the coherence time. For a π-pulse duration of $\tau_\pi = 75\mu sec$, as shown in Fig. 27 the coherence time measured for is $\tau_{coh} = 29 \pm 9msec$. Another measurement with $\tau_\pi = 300\mu sec$ resulted in $\tau_{coh} = 70 \pm 15msec$.

In a Ramsey experiment a $\frac{\pi}{2}$-pulse with $5kHz$ detuning with respect to the clock transition was applied followed by a period of time with zero RF power which

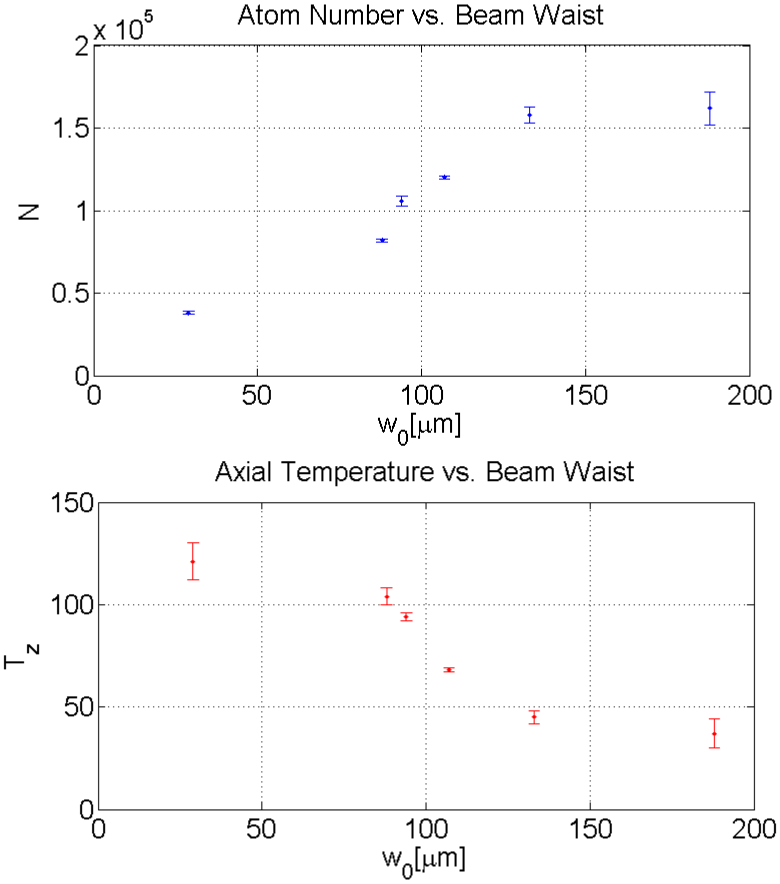

Fig. 26: Atom number and axial temperature as a function of the beam waist. Measurements were performed after a trapping time of $250msec$ and trapping power of $18W$.

is followed by another $\frac{\pi}{2}$-pulse pulse. This results in Ramsey oscillations with much shorter coherence times. For a $\frac{\pi}{2}$-pulse time of $\tau_{\frac{\pi}{2}} = 10\mu sec$ the Ramsey coherence time measurement yields $\tau_{coh} = 4.7 \pm 0.7msec$. The measurement and fit are presented in Fig. 28

6 Concluding Remarks

Our goal in the full experiment is to be able to achieve BEC of the ^{87}Rb atoms. However, the characterization of the CO_2 dipole trap, along with more evidence concerning the performance of the MOT, made us reach the conclusion that reach-

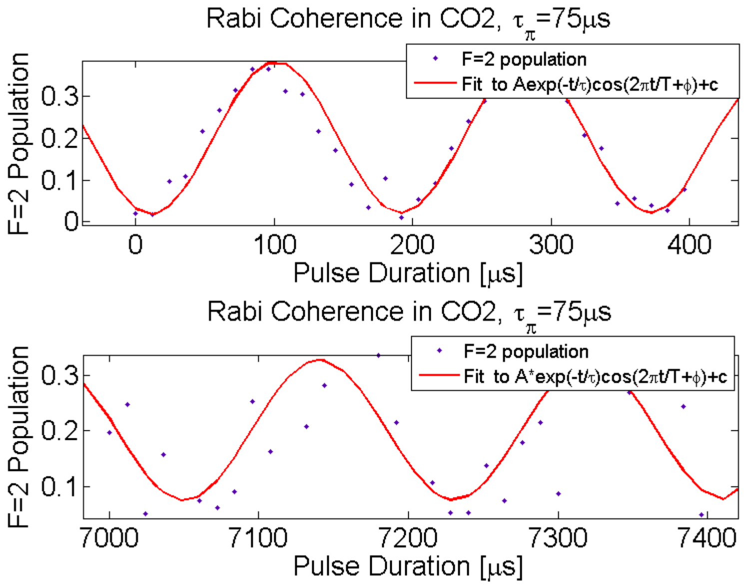

Fig. 27: Rabi oscillations in two time ranges. The dots represent the data and the solid line is a fit of the data to decaying oscillations. The coherence time is $\tau_{coh} = 19 \pm 9msec$.

ing BEC in the our apparatus was implausible due to poor vacuum conditions, as discussed below.

6.1 CO_2 Trap Performance

Our maximal initial CO_2 size was 2.5×10^5, which is an order of magnitude smaller than the traps in the works of Weitz and Ott [18, 16] with size of a few times 10^6. Typically the time it takes to perform evaporation is no less than $5sec$. With lifetime of $500msec$ such as in our trap evaporation is impractical due to the atom loss. The steady state temperature of $100 - 120\mu K$ after $200msec$ as shown in Fig. 24 indicates that the atom loss after thermalization is not due to evaporation or heating of the trap, since both would have changed the temperature. Thus the most probable cause for the short lifetime is the background pressure kicking atoms out of the trap.

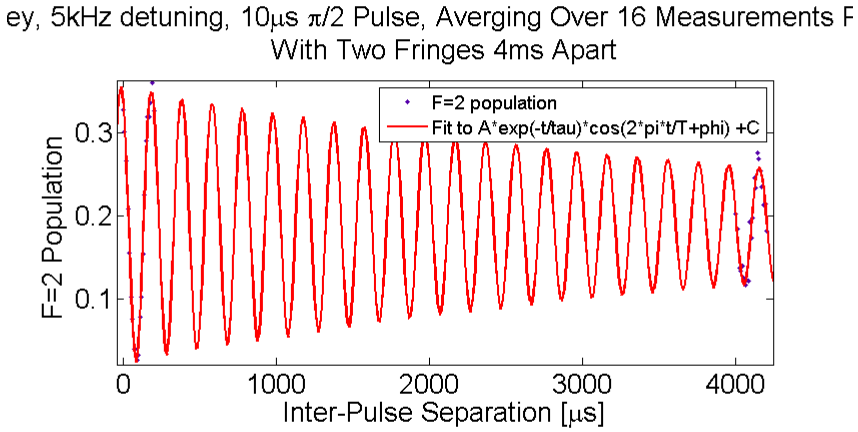

Fig. 28: Ramsey oscillations in two time ranges. The dots represent the data and the solid line is a fit of the data to decaying oscillations. The coherence time is $\tau_{coh} = 4.7 \pm 0.7msec$. The oscillations period is $T = 198.4 \pm 0.2\mu sec$.

References

[1] C. Cohen-Tannoudji, *"Atomic Motion in Laser Light - Course 1"*, available online at http://www.phys.ens.fr/~cct/articles/cours/atomic-motion-in-laser-light-1992.pdf

[2] J. R. Ackerhalt and J. H. Eberly, *Quantum electrodynamics and radiation reaction: Nonrelativistic atomic frequency shifts and lifetimes*, Phys. Rev. **D** 10, 3350–3375 (1974).

[3] Daniel A. Steck, *Rubidium 87 D Line Data*, available online at http://steck.us/alkalidata (revision 2.1.4,23 December 2010).

[4] E. Joos and H.D. Zeh, *The emergence of classical properties through interaction with the environment*, Z. Phys. **B** 59, 223.

[5] Rudolf Grimm, Matthias Weidemüller, and Yurri B. Ovchinnikov. *Optical dipole traps for neutral atoms.* xxx.lanl.gov - physics/9902072, 1999.

[6] T. Takekoshi, J.R. Yeh and R.J Knize, *Quasi-electrostatic trap for neutral atoms*, Opt. Comm. 114, 421 (1995).

[7] T. Takekoshi and R. J. Knize, *Co2 laser trap for cesium atoms*, Optics Lett. 21, 77 (1996) .

[8] E. Raab, M. Prentiss, A. Cable, S. Chu, and D. Pritchard. *Trapping of neutral sodium atoms with radiation pressure*, Phys. Rev. Lett. 59 2631, (1987).

[9] K. E. Gibble, S. Kasapi, and S. Chu. *Improved magneto-optic trapping in a vapor cell.* Optics Letters, 17(7):526–528, (1992).

[10] K. Lindquist, M. Stephens, and C. Wieman. *Experimental and theoretical study of the vapor-cell zeeman optical trap*, Phys. Rev. **A**, 46:4082, (1992).

[11] T. Walker, D. Sesko, and C. Wieman. *Collective behaviour of optically trapped neutral atoms*, Phys. Rev. Lett. 64(4):408–411, (1990).

[12] Marshall T. DePue, S. Lukman Winoto, D.J. Han, David S. Weiss, *Transient compression of a MOT and high intensity fluorescent imaging of optically thick clouds of atoms*, Opt. Comm. 180:73–79 (2000).

[13] C. Monroe, Swann, H. Robinson, and C. Wieman, *Very Cold Trapped Atoms in a Vapor Cell.* Phys. Rev. Lett. 65, 1571–1574 (1990).

[14] Y. Dallal, PhD. Interim Report, *Interactions Between Cold Ions and Ultra-Cold Atoms in Overlapping Traps*, Weizmann Instituite of Science (December 21, 2011).

[15] Svelto, Orazio, and D. C. Hanna, *Principles of Lasers*, New York: Plenum Press. (1998) ISBN: 0-306-45748-2.

[16] T. Gericke, P. Wuertz, D. Reitz, C. Utfeld, H. Ott, *All-optical formation of a Bose-Einstein condensate for applications in scanning electron microscopy*, Appl. Phys. **B** 89, 447–451 (2007).

[17] Amnon Yariv, *Quantum Electronics 3rd edition*, ISBN: 0-471-60997-8.

[18] G. Cennini, G. Ritt, C. Geckeler and M. Weitz, *Bose–Einstein condensation in a CO2-laser optical dipole trap*, Appl. Phys. **B** 77, 773–779 (2003).

[19] C. K. N. Patel, *Continuous-Wave Laser Action on Vibrational-Rotational Transitions of CO2*, Phys. Rev. 136, A1187-A1193 (1964).

[20] http://www.windows2universe.org/earth/climate/greenhouse_effect_gases.html.

[21] E. A. Donley, T. P. Heavner, F. Levi, M. O. Tataw, and S. R. Jefferts, *Double-pass acousto-optic modulator system*, Rev. Sci. Instrum. 76, 063112 (2005).

[22] W. Ketterle, D. S. Durfee, and D. M. Stamper-Kurn, *Making, probing and understanding bose-einstein condensates*, cond-mat, 9904034v2, (1999).

[23] D. S. Weiss, E. Riis, Y. Shevy, P. Jeffery Ungar, and S. Chu. *Optical molasses and multilivel atoms: experiment*, J. Opt. Soc. Am. **B**, 6(11):2073, (1989).

[24] N. R. Newbury, C. J. Myatt, and C. E. Wieman, *s -wave elastic collisions between cold ground-state 87Rb atoms*, Phys. Rev. **A**, 51:R2680–R2683, Apr (1995).

[25] F. Dalfovo et al., Rev. Mod. Phys. 71, 463 (1999).

[26] M. H. Anderson et al., Science 269, 198 (1995).

[27] D. F. V. James, *Quantum dynamics of cold trapped ions with application to quantum computation*, Appl. Phys. **B** 66, 181 (1998).

[28] J. N. Tan, J. J. Bollinger, B. Jelenkovic, andD. J.Wineland, *Long-range order in lasercooled, atomic-ion Wigner crystals observed by Bragg scattering*, Phys. Rev. Lett. 75, 4198 (1995).

[29] D. H. Dubin and T. M. ONeil, *Trapped nonneutral plasmas, liquids, and crystals*, Rev.Mod. Phys. 71, 87 (1999).

[30] M. Cetina et al., *Bright source of cold ions for surface-electrode traps*, Phys. Rev. A 76, 041401 (2007).

[31] A. T. Grier et al., *Observation of Cold Collisions between Trapped Ions and Trapped Atoms*, Phys. Rev. Lett. 102, 223201 (2009).

[32] Stefan Schmid, Arne Harter and Johannes Hecker Denschlag *Dynamics of a Cold Trapped Ion in a Bose-Einstein Condensate*,Phys. Rev. Lett. 105, 133202 (2010).

[33] Christoph Zipkes, Stefan Palzer, Lothar Ratschbacher, Carlo Sias and Michael Kohl, *Cold Heteronuclear Atom-Ion Collisions*, Phys. Rev. Lett. 105, 133201 (2010).

[34] R. Cote, *From Classical Mobility to Hopping Conductivity: Charge Hopping in an Ultracold Gas*, Phys. Rev. Lett. 85, 5316 (2000).

[35] R. Cote and A. Dalgarno, Phys. Rev. **A**, *Ultracold atom-ion collisions*, 62, 012709 (2000).

[36] O. P. Makarov, R. Cote, H. Michels and W. W. Smith, *Radiative charge-transfer lifetime of the excited state of (NaCa)+*, Phys. Rev. **A** 67, 042705 (2003).

[37] Z. Idziaszek, T. Calarco, and P. Zoller, *Controlled collisions of a single atom and an ion guided by movable trapping potentials*, Phys. Rev. **A** 76, 033409 (2007).

[38] Z. Idziaszek, T. Calarco, P. S. Julienne, A. Simoni, *Quantum theory of ultracold atom-ion collisions* , arXiv:0806.4002 (2008).

[39] R.V. Krems, *Cold controlled chemistry*, Phys. Chem. Chem. Phys. 10, 4079 (2008).

[40] R. Cote, V. Kharchenko, and M. D. Lukin, *Mesoscopic Molecular Ions in Bose-Einstein Condensates*, Phys. Rev. Lett. 89, 093001 (2002).

[41] M. D. Barrett, J. A. Sauer, and M. S. Chapman, *All-Optical Formation of an Atomic Bose-Einstein Condensate*, Phys. Rev. Lett. 87, 010404 (2001).